LONG-RANGE DESCRIPTION OF RHEOLOGICAL PROPERTIES OF A HIGH-PRESSURE HIGH-TEMPERATURE OIL-BASED DRILLING FLUID

A Thesis

by

RAFAEL CESAR TEIXEIRA OLIVEIRA

Submitted to the Office of Graduate and Professional Studies of
Texas A&M University
in partial fulfillment of the requirements for the degree of

MASTER OF SCIENCE

Chair of Committee,	Jerome Schubert
Committee Members,	Mahmoud El-Halwagi
	Samuel Noynaert
Head of Department,	Daniel Hill

August 2016

Major Subject: Petroleum Engineering

ABSTRACT

Drilling teams face several challenges when operating in high-pressure, high-temperature (HPHT) fields, such as lost circulation and difficulties in well control. One way to address these issues is to fully understand the rheological properties of the drilling mud being used at the temperature and pressure conditions observed in the formation. Operationally, this may not only help to increase drilling efficiency and reduce its costs, but also in avoiding wellbore instability and loss of drilling fluids.

Aiming to investigate the behavior and apply novel models that closely describe the rheological properties of an oil-based drilling fluid under larger than previously described HPHT intervals in the literature, this research uses formerly obtained experimental data to develop models for dynamic viscosity, shear stress, 10s gel strength, 10min gel strength, yield point, flow behavior index and flow consistency index as a function of temperature, pressure and, where applicable, shear rate. These models, unlike other works currently available in the literature for HPHT drilling fluid rheology, allow for robust prediction of fluid behavior in virtually any condition in the HPHT section of a wellbore, including shear rate.

DEDICATION

For my parents, Marcia and Reinaldo, for all their love and support.

ACKNOWLEDGEMENTS

I would like to thank my committee chair, Dr. Schubert, and my committee members, Dr. El-Halwagi and Dr. Noynaert, for their guidance and support. Without you this work could not have come to be.

Thanks also to my friends from Texas A&M, in particular those from AADE, BRSA, Coisinhas and my former roommates. You turned an academic opportunity into an unforgettable life experience.

Finally, I would like to extend my gratitude to CAPES Foundation and the Ministry of Education of Brazil for the financial support through the scholarship process 88888.075990/2013-00.

NOMENCLATURE

10s GS	10-second gel strength
10min GS	10-minute gel strength
γ	Shear rate
μ	Dynamic viscosity
ρ	Density
τ	Shear stress
υ	Kinematic viscosity
ANOVA	Analysis of variance
BOP	Blowout preventer
HPHT	High-pressure high-temperature
K	Flow consistency index
n	Flow behavior index
OBM	Oil-based mud
PV	Plastic Viscosity
WBM	Water-based mud
YP	Yield point

TABLE OF CONTENTS

Page

LIST OF FIGURES

Page

LIST OF TABLES

Page

1. INTRODUCTION

With the current trend of drilling for hydrocarbons in ever-increasing depth, both temperature and pressure may reach extreme values. Several complications may arise from this, especially related to drilling fluids and their properties: difficulty in predicting hydrostatic pressures in high-pressure/high-temperature (HPHT) environments (Zamora, Roy, Slater, & Troncoso, 2013) and thermal instability (Lee & Shadravan, 2012; Zhou, Deville, & Davis, 2015), and also their consequences, such as kicks, loss of drilling fluids, wellbore instability (Demirdal & Cunha, 2009) and wellbore cleanup hurdles (Shadravan & Amani, 2012).

These challenges became more conspicuous after the Macondo well blowout in the Gulf of Mexico: an explosion and fire struck the platform Deepwater Horizon, which ultimately sunk 36h after the incident (Skogdalen, Utne, & Vinnem, 2011). Eleven workers died in the accident (Kaufman, 2010) and, for almost three months, oil leaked into the ocean in quantities estimated in the order of millions of stock tank barrels (Griffiths, 2012), leaving the operating company, BP, with a multibillion dollar settlement in compensation to federal, state and local governments for the oil spill (British Petroleum, 2015). The vast proportions of this accident demonstrate how crucial it is to holistically understand the processes and the risks involved in HPHT drilling. One way to address that is through the understanding of drilling fluids and their properties. Their behavior is of great import in order to reduce not only risks associated with HPHT

wells, but also in order to increasing efficiency and reducing the associated costs (Bland, Mullen, Gonzalez, Harvey, & Pless, 2006).

There is copious information about drilling fluid rheology, but not so much under HPHT conditions, and models based on the limited pressure and temperature intervals tend to be considerably inaccurate. For example, Bland, Mullen, Gonzalez, Harvey, & Pless (2006) carried out extrapolations of a third-degree model constructed with historically available drilling fluid data up to 20,000 psi. For the interval to which they fit the model, the authors obtained good approximations. However, when brought up to 30,000 psi, it presented significant compression overestimations when contrasted to results obtained in laboratory tests. Therefore, as also indicated in the work of Amani & Al-Jubouri in An Experimental Investigation of the The Effects of Ultra High Pressures and Temperatures on the Rheological Properties of Water-Based Drilling Fluids (2012), the extrapolation of properties measured at surface conditions to downhole conditions may prove to be unreliable.

This work aims to address this issue. By means of analysis and development of improved models to HPHT rheology test data, this work will fit models to the dynamic viscosity (μ), shear stress (τ), 10s gel strength (10s GS), 10min gel strength (10min GS), yield point (YP), flow behavior index (n) and flow consistency index (K) of an HPHT, heavy-weight, oil-based mud sample with characteristics similar to those currently utilized in drilling of prospects and fit models, enabling robust prediction of its behavior in the HPHT interval.

2. LITERATURE REVIEW

2.1. Drilling fluids

Drilling fluids constitute an essential part of drilling. And that is no surprise, considering that they are responsible, among other functions, for: (1) removing cuttings, or rock fragments, that originate from drilling activities; (2) cooling and, through lubrication, reducing friction of the rotating bit and drillstring; (3) controlling fluid-loss through the formation of a filter cake along the borehole walls; (4) controlling eventual well-control issues through overbalance, that is, the mud exerting a higher pressure than that observed in the formation; (5) supporting the drillstring and casing weight, essentially through buoyancy; and (6) communicating the exerted hydraulic force to the bit, which happens as the mud flows through the bit nozzles, thus rotating the latter and powering measurement-while-drilling and other tools (Eustes, 2011).

Therefore, it should also be no surprise that drilling fluids are considered to be, either directly or indirectly, related to most drilling problems. Selection of an appropriate mud system is, then, imperative to drilling enterprises, and it will be a function of, for example, the types of formations the team will drill through, the formation's temperature, pressure, pore pressure, strength and permeability intervals, and environmental concerns (Bourgoyne, Millheim, Chenevert, & Young, 1991).

In a broad but useful fashion, drilling fluids are classified as non-water-based fluids, water-based fluids and pneumatic fluids (Ibeh, 2007). Some (Bourgoyne, Millheim, Chenevert, & Young, 1991; Eustes, 2011) stated that water-based muds

(WBM) are typically the cheapest, the most commonly used and that they present good characteristics to prevent mud losses. On a not so positive note, they may lead to time-dependent borehole issues and are also reactive to clays. Another option, the use of pneumatic fluids, became favorable in the 1990s with the development of underbalanced drilling, leading to simpler completion procedures and reduced work-over, though it may incur in higher costs and bring about additional safety concerns. Finally, within non-water-based fluids, there is the big branch of oil-based muds (OBM), which are typically formulated with diesel. Though these present themselves with some environmental concerns and may be costlier than other mud systems – at least upfront --, they present greatly improved performance and stability, especially at higher temperatures. This means that they can perform well even where those, like WBM, would chemically fail due to too high temperatures. In addition, they are highly and intrinsically inhibitive, and provide enhanced lubricity.

This research will be elaborating on OBM fluids under HPHT conditions.

2.2. OBM and WBM in HPHT drilling

OBM and WBM are considered the most common types of drilling fluids used and they both present good characteristics for drilling, although there seems to exist a preference for OBM when drilling HPHT prospects. Mahmood, Al-Jubouri, & Shadravan (2012) carried out a study in which they contrasted the rheological properties of OBM and WBM at temperatures and pressures ranging from 100 to 600°F and from 5,000 to 25,000 psi, respectively. The authors found that the OBM tested presented higher resistance to HPHT conditions than the WBM tested, demonstrating a failure

temperature at about 400°F for the former and 250°F for the latter. Naturally, OBM pose a higher environmental threat when compared to WBM, since they contain environmentally detrimental components.

Ibeh (2007) made similar observations in his study. The author stated that some of the other positive aspects of OBM, apart from temperature stability, consist in the fact that they present superior lubricity when contrasted to WBM and are able to maintain a stable rheology and filtration control.

The composition relative to additives may be somewhat similar in OBM and WBM, except, of course, for the essential difference in the base fluid. Some even use water-in-oil emulsion, which presents water droplets dispersed in the oil phase (Bourgoyne, Millheim, Chenevert, & Young, 1991). However, diesel- and synthetic-based mud with no water in emulsion still prevail in prospects where the drilling team will have to drill through long, horizontal sections where the salt concentrations present in the formation water is variable, thus enhancing stability (Eustes, 2011).

2.3. Differences between regular and HPHT drilling

There are several definitions in the literature as to what comprises HPHT drilling. However, the most commonly found definition states that, basically, HPHT environments entail formations with pressure values larger than 10,000 psi and temperatures that exceed 300°F (Shadravan & Amani, 2012).

For non-HPHT wells, neglecting the influence of temperature and pressure on mud weight is typically not a problem. That is, downhole pressures estimated with true vertical depth and the mud weight measured at the surface are common practice and do

not incur serious deviations. For HPHT wells, on the other hand, the effects of temperature and pressure are considerable and should not be disregarded. Thus, carrying out corrections for compression and expansion becomes necessary (Bland, Mullen, Gonzalez, Harvey, & Pless, 2006; Ibeh, 2007).

When drilling in HPHT environments, a higher mud weight may be necessary, and that is accomplished by increasing the amount of dispersed weight material, such as barite, manganese tetroxide, siderite, calcium carbonate, hematite, ilmenite and galena. There are, however, several implications of using heavier mud when drilling, i.e., increasing the mud density. Noticeably, the horsepower available at the bit is significantly reduced, as well as the efficiency in cutting (Bland, Mullen, Gonzalez, Harvey, & Pless, 2006; Eustes, 2011).

2.4. Other difficulties associated with HPHT drilling

There are several challenges facing a drilling team when working on an HPHT well, and these range from well control and reliability of electronics to safety issues.

2.4.1. Electronic components under high temperatures

Most of the electronic equipment is rated to 158, 185 and 257°F, but that is insufficient for measurement while drilling and for rotary steerable systems in HPHT environments, where temperatures may reach 400°F or above. And high temperatures are not the only source of damage and malfunction; there is also the fact that there are high vibration levels. Thus, the reliability of electronic components becomes a concern as reservoirs grow deeper and deeper (Ahmad, et al., 2014).

It is important to understand that most electronic systems are very complex, with a vast number of different parts found in a single piece of equipment. Seeking to improve the reliability of electronics, many tests can be carried out, ultimately increasing both the lifetime and the performance at high temperatures. Basically, one way to approach this is carrying out tests in three steps: first, running a test above or at the maximum operating temperature and identify failing parts; second, replacing failing parts with an alternative; and third, submitting tools to a long-term test to validate the improvements in the electronic device. Carrying out this procedure, Ahmad et al. (2014) were able to quadruple the expected lifetime of an electronic system at approximately 350°F.

There is another measure that can be taken in order to increase the expected lifetime of electronic parts at HPHT conditions: mud cooling. It is considered economically and technically feasible, and has great positive impacts, since it reduces the downhole temperature. Mud cooling is typically carried out through heat exchangers (Ahmad, et al., 2014).

2.4.2. Inadequacy of conventional drilling

Conventional drilling consists basically of maintaining the downhole hydrostatic pressure with the drilling fluid, or mud. The fluid column along the drillstring, at least ideally, should present a downhole pressure that is below that of the formation, but above that of the pore pressure (Elliott, Montilva, Francis, Reitsma, Shelton, & Roes, 2011). If one is conventional overbalanced drilling in HPHT environments, several significant disadvantages may arise while developing such prospects. For example, the

small margin between the pore and fracture pressure makes it difficult for conventional drilling to reach the total depth without substantially damaging the formation (Demirdal & Cunha, 2009). In fact, this narrow operating margin may lead to an economically unfeasible well if a large number of casings need to be run (Santos, Leuchtenberg, & Sara, 2003), ultimately limiting production.

These difficulties experienced when conventionally drilling gave rise to two other methods: underbalanced drilling (UBD) and managed pressure drilling (MPD). UBD is defined as a drilling process in which the pressure applied to the open-hole is below that of the formation, and is done with the intent of bringing formation fluids to the surface (International Association of Drilling Contractors, 2005). It was first developed in order to help the drilling process, but it was then discovered that it also minimized damage to the reservoir. The high costs associated with this technology as well as some impediments to applying it in offshore prospects, however, kept UBD from ubiquitous application. In order to address these issues, MPD was developed. It can be understood as being an intermediary between conventional drilling and UBD (Ostroot, Shayegi, Lewis, & Lovorn, 2007), where the open-hole pressure is maintained at or slightly above the pore pressure, thus avoiding flow into the wellbore. This is achieved through a set of techniques and equipment, which ultimately avoid setting case as often as overbalance drilling requires (Rehm, Schubert, Haghshenas, Paknejad, & Hughes, 2008; Ostroot, Shayegi, Lewis, & Lovorn, 2007).

2.4.3. Safety issues concerning HPHT drilling

There are several concerns related to safety in HPHT drilling. Kick prevention and kick detection are main safety issues faced in HPHT prospects. Kicks often occur as the drilling assembly is pulled out of the hole, which can be attributed to swabbing: the effect of decreasing the pressure at the bit when removing the drilling assembly. Other events that often precede kicks are coring (small space between the open hole and the core barrel, which may also cause swabbing), connections (when mud flow stops and the equivalent circulating density equals the hydrostatic pressure, gas may permeate to the open hole) and lost circulation (mostly due to small difference between the pore and fracture pressure in the given formation). Kick detection still mostly occurs through mud level measuring in the mud pits, but operators currently can also analyze acoustic pulses the mud pumps generate: the presence of gas in the annulus alters the travel speed of the pump-generated pulses, which sets off an alarm. (Shrivastav, 2012).

It is also worthwhile mentioning that kick detection when using an OBM may be considerably more difficult than what it would be if using a WBM. Pit gains are considerably smaller with the former, and that is due to the fact that gas in the formation solubilized in the mud, thus reducing pit gains. How much gas will enter the mud will depend on several factors, such as the composition of the gas and the kind of base oil used in the mud. Also, solubility will increase the (1) higher the density of the gas, (2) the lower the density of the oil, (3) the higher the pressure and (4) the lower the temperature. (Bland, Mullen, Gonzalez, Harvey, & Pless, 2006)

Additionally, blow-out preventer (BOP) technology is an area where there is still great room for improvement. Current high-specification 18 ¾ BOP operating limits are of 15,000 psi and 250°F, values insufficiently low for many of the recent HPHT prospects (Patel, Bruton, & Buchanan, 2015).

Down-hole electronic equipment may also suffer from high temperatures, especially as these approach or surpass their operating limit. Automated drilling relies heavily on vast amounts of data, but the conditions to which machinery might be subject to in HPHT prospects jeopardizes not only the reliability of the data, but also their functioning (Ahmad, et al., 2014).

One way to mitigate hot down-hole temperatures is through mud cooling. El Dorry, Coit, Gutierrez, Woolums, & Herrington (2015), in a study involving 5 wells, used a closed-loop mud cooler in South Texas. The authors reported three main positive aspects of applying the system: longer sections were drilled before reaching the critical circulating temperature of 300°F; bottom hole temperature was roughly 20°F lower than estimated temperatures without the mud cooling system; and considerably less time was necessary to lower the well temperature once the critical circulating temperature was reached, saving a calculated 51 hours per well. The authors also explain that cooler mud improves safety for personnel in charge of mud sampling and monitoring.

2.4.4. Slow rate of penetration

Proehl & Sabins (2006) reported considerable reduction in the rate of penetration in HPHT environments when contrasted to ordinary drilling environments. They estimated that the bits operating in the former environment remove, per rotation, only a

tenth of the rock when compared to the latter. According to the authors, this may be due to many factors, such as low torque, impregnated cutter and use of roller-cone bits, which were deemed unsuitable for HPHT wells.

2.5. Fundamentals of rheology

The field of rheology first came to be around 1930. Bair (2007), in a concise fashion, defines it as being

"(...) the study of deformation and flow of materials."

Basically, the unusual behavior of various materials was the ignition point of studies in this field. Many materials that one could describe as solid or liquid present, respectively, fluid-like or solid-like characteristics and, thus, such classifications are insufficient to describe them. These so called fluid-like and solid-like properties are an indication of time dependence, i.e., the obtained results in rheological tests will depend on a time scale. Hence the importance of consistently describing the observed changes in materials. Their properties, studied by rheology, are typically described as models, useful in both qualitative and quantitative analysis. (Malkin & Isayev, 2006).

The first mathematical descriptions of liquid and solid behavior are dated back to Isaac Newton and Robert Hooke, respectively. The former, by spinning a cylinder in a vessel, observed that deformation rates in certain liquids are proportional to the applied stress. The proportionality constant to this relation is denominated viscosity. The latter described something similar, though for solids. While both these models define with considerably good accuracy the behavior of a number of materials, there are many others

that do not follow such patterns: they are denominated non-Newtonian or non-Hookean. These are the materials that rheology studies (Malkin & Isayev, 2006).

The definition of rheology Bair (2007) provided, though useful, may prove to be significantly ambiguous. Malkin & Isayev (2006) stress that such definition is similar to continuum mechanics, not actually characterizing the particularities of rheology. The latter authors provide in their work a succinct, yet thorough, analysis of what rheology and rheological properties consist in:

> *"Rheology is a science concerned with mechanical properties of various solid-like, liquid-like, and intermediate technological and natural products. It accomplishes its goals by means of models representing principal peculiarities of behavior of these materials. The behavior of material is a relationship between forces and changes of shape. A model gives a mathematical formulation of such relationship. Rheological properties are expressed by the model structure (i.e., its mathematical image) and values of constants included in the model are characteristics of material."*

2.5.1. Viscosity

As previously stated, there are materials that present fluid-like and solid-like properties. But what is a fluid? Fluids encompass gases, liquids and vapors (Fox, McDonald, & Pritchard, 2004). Mohanty (2006) describes them as materials that, whilst under the effect of the external shearing force, present continuous deformation and, once the shearing effects are terminated, deformation ceases and the materials do not return to their original state. A corollary of this definition then is that a fluid cannot sustain shear forces. Solids, on the other hand, do not present this time-dependent deformation upon

application of shear stress. When a solid bar of a given material is subjected to a monotonically increasing stress along a single axis, given that the elastic limit of the given solid is not surpassed, the deformation the body undergoes is proportional to the applied stress. Additionally, the body will return to its original state once the applied stress ceases (Fox, McDonald, & Pritchard, 2004; Ragab & Bayoumi, 1998).

For fluids in different states, viscosity varies in different ways. For gases presenting low densities, viscosity typically increases with increasing temperatures, whereas for liquids the behavior observed is normally the opposite, decreasing viscosity with increasing temperature. This is mostly due to how these phases act in an intermolecular level: gases carry momentum in between collisions, as the molecules are almost in a free flight. On the other hand, liquids maintain their relative cohesion (in a laminar flow) while carrying momentum through interactions with their neighboring molecules (Bird, Stewart, & Lightfoot, 2002).

2.5.2. Dynamic viscosity

Fluids present a property called dynamic (or absolute) viscosity. One way to understand it is through the application of shear forces to a fluid in between parallel two plates, as displayed in Figure 1. This system is initially at rest (a), but, as the top plate starts to move at a constant velocity and parallel to the opposing plate (b), the fluid acquires momentum (c). It is worthwhile mentioning that the speed at which the top plate moves must be slow enough to ensure a laminar flow in order to observe such results. Ultimately, the system will reach a linear steady-state velocity profile (d) and,

once this takes place, a constant force F will maintain the motion of the top plate. The expression that describes this experiment is given by

$$\frac{F}{A} = \mu \frac{V}{Y} \qquad (1)$$

where F is the constant force applied, A is the area of the plate, Y is the distance between the two plates, V is the velocity and μ is the constant of proportionality for the given fluid, called dynamic viscosity. Its units in SI are $^{kg}/_{m.s}$ or simply $Pa.s$. Alternatively, in oilfield units it is given in cP (Bird, Stewart, & Lightfoot, 2002). Table 1 presents the dynamic viscosity of common liquids at 14.7 psi and 68°F.

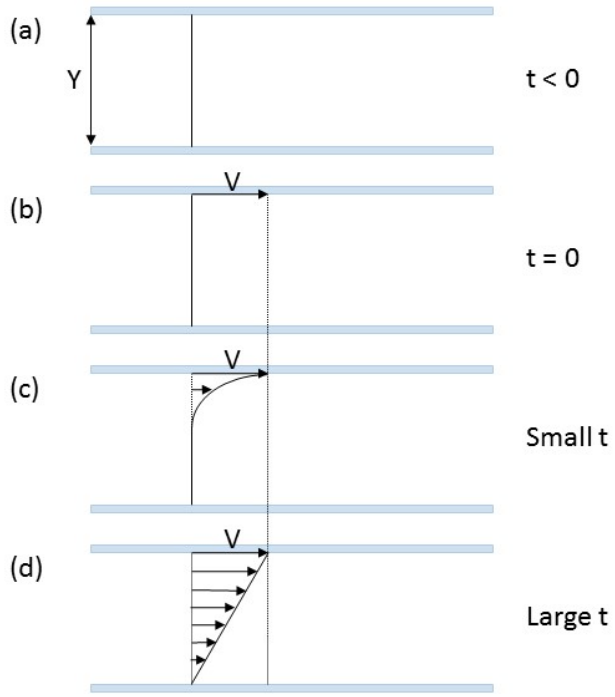

Figure 1. Shear forces on fluid between parallel plates when (a) fluid is at rest; (b) top plate starts to move at constant speed; (c) fluid acquires momentum; (d) the system reaches a steady state velocity profile. (Bird, Stewart, & Lightfoot, 2002)

Table 1: Dynamic viscosity of common liquids at 14.7 psi and 68°F. (White, 2006)

Liquid	μ, cP
Ammonia	0.220
Benzene	0.651
Ethanol	1.20
Gasoline	0.292
Glycerin	1490
Kerosene	1.92
Methanol	0.598
SAE 10W oil*	104
SAE 10W30 oil*	170
SAE 30W oil*	290
SAE 50W oil*	860
Water	1.00

*Representative values. The SAE oil classifications accept deviations as high as ±50%.

From Eq. (1) originates what is frequently called Newton's law of viscosity: τ_{yx}, described as the force in the x direction on a unit area, which is perpendicular to the y direction, replaces $^{F}/_{A}$. In other words, τ_{yx} is the force the fluid with a smaller y value (as presented in Figure 1) exerts on the fluid with a larger y value. Additionally, $^{V}/_{Y}$ gives way to $^{-dv_x}/_{dy}$ (Bird, Stewart, & Lightfoot, 2002). Newton's law of viscosity is thus expressed as

$$\tau_{yx} = -\mu \frac{dv_x}{dy} \qquad (2)$$

Eq. (2) indicates that there is a proportionality that relates the velocity gradient in the flow to the shearing force per unit area.

2.5.3. Kinematic viscosity

The kinematic viscosity is defined as

$$\nu = \frac{\mu}{\rho} \qquad (3)$$

where ρ is the fluid's density. This ratio occurs often in fluid mechanics and, thus, the symbol ν is associated with it. Kinematic viscosity is given in SI in m^2/s (Fox, McDonald, & Pritchard, 2004).

2.6. Yield point

Another important property in the realm of rheology is the yield point (YP). It is a parameter present in the Bingham plastic model – developed in Section 2.8.5. Graphically, YP is the zero-shear-rate intercept on a shear stress versus shear rate plot. Physically, it is obtained from the subtraction of the PV (viscometer dial reading at 600 RPM minus the reading at 300 RPM) from the 300 RPM viscometer dial readings, and in oilfield units it is given in $lbf/100ft^2$ (Amani, The Rheological Properties of Oil-Based Mud Under High Pressure and High Temperature Conditions, 2012).

In other words, from a drilling engineer's perspective, it can be thought of as a way to quantify how good a mud is to lift cuttings out of the hole: higher values imply in better cut-lifting properties. It is important to understand that the presence of a yield point necessarily indicates that the fluid is non-Newtonian-like (Amani, The Rheological Properties of Oil-Based Mud Under High Pressure and High Temperature Conditions, 2012).

2.7. Gel strength

Also related to rheological measurements is a property denominated gel strength, which focuses in measuring a fluid's shear stress at low shear rates after the fluid is let sit quiescently for a certain period of time. API recommended procedures suggest this period be of 10 seconds and 10 minutes. This property, just as YP, is also given in $lbf/100ft^2$ (Amani, The Rheological Properties of Oil-Based Mud Under High Pressure and High Temperature Conditions, 2012).

2.8. Rheological models

Before stepping into rheological models, it is important to understand the concept of thixotropy. Although there is some controversy related to its definition, since the general meaning and use of the word thixotropy has changed over time, Barnes, through Thixotropy - a review, (1997), in a thorough and detailed review, narrowed its definition basically to being a characteristic associated with the behavior of non-Newtonian fluids. Essentially, it is a property of fluids that present a time-dependent, reversible decrease in their viscosity as they are subject to flow (Møller, Mewis, & Bonn, 2006). Due to their time-dependence, thixotropic measurements are best executed through equilibrium readings. Savins & Roper (1954), in a classic study on viscosity readings and drilling fluids, explained:

> *"When a sample of thixotropic drilling fluid is sheared at a constant rotor speed in any rotating cylinder viscometer, the torque readings usually change at a decreasing rate until an equilibrium torque reading is obtained. (...) The equilibrium toque reading is*

obtained when the thixotropic structure has reached a steady state for that particular rotor speed."

And there are numerous models that follow this procedure to attempt to describe fluid behavior at various conditions. These are constructed through data regression obtained with rheometers. It is important to understand, however, that these models are not appropriate to predict every fluid's behavior and thus, if collected data does not match the model function, it is best to find a more suitable model function. This work presents some of the most adopted models: Newtonian, Oswald/de Waele, Carreau/Yasuda, Herschel/Bulkley and Bingham Plastic (Mezger, 2006). Figure 2 graphically demonstrates the general behavior fluids that follow some of these models through a shear stress versus shear rate plot.

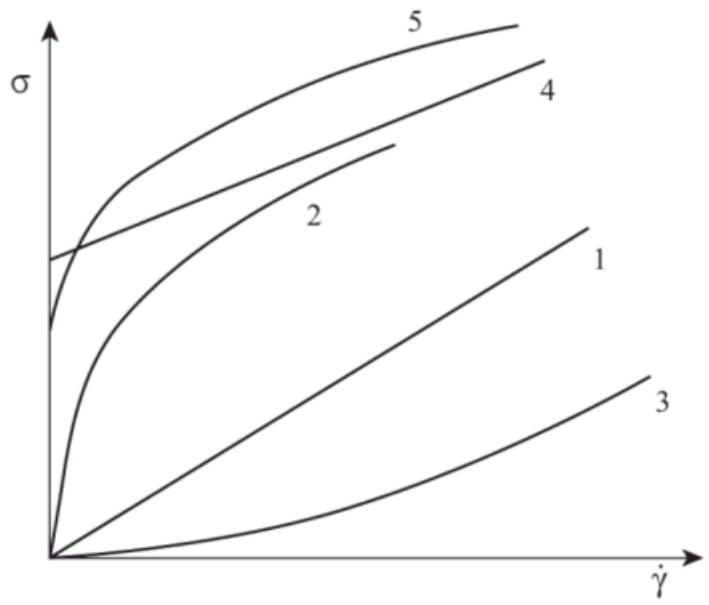

Figure 2. A generalized behavior of various fluids on a shear stress (y-axis) versus shear rate (x-axis): (1) Newtonian fluid, (2) Oswald/de Waele shear thinning fluid, (3) Oswald/de Waele shear thickening fluid, (4) Bingham fluid and (5) Herschel Bulkley fluid. (Mewis & Wagner, 2012)

2.8.1. Newtonian model

This is the model function appropriate for fluids that present an ideally viscous (idealviscous) flow behavior. Basically, it consists in Eq. (2) displayed in a different fashion, where γ, denominated shear rate, given in s^{-1}, substitutes the term $-{}^{dv_x}/_{dy}$ (Mezger, 2006). Thus, it is rewritten as

$$\tau = \mu\,\gamma \qquad (4)$$

Most drilling fluids, however, do not follow this model function.

2.8.2. Oswald/de Waele model

The Ostwald/de Waele model, or Power-law model, follows the expression

$$\tau = c\,\gamma^{p} \qquad (5)$$

where c is the flow coefficient, or consistency index, $Pa.s^p$, p is the power-law index, dimensionless, and γ is the shear rate, s^{-1}. In fact, the power-law index indicates if the flow is shear-thinning ($p < 1$), shear thickening ($p > 1$) or idealviscous ($p = 1$) (Mezger, 2006). If the given fluid presents idealviscous behavior, then Eq. (5) becomes identical to Eq. (4) and the flow behavior matches that of the Newtonian model.

2.8.3. Carreau/Yasuda model

Carreau/Yasuda is a model function that comprises zero-shear and infinite-shear viscosity, respectively, in the following manner

$$\eta_0 = \lim_{\gamma \to 0} \eta(\gamma) \quad (6)$$

$$\eta_\infty = \lim_{\gamma \to \infty} \eta(\gamma) \quad (7)$$

Inadequate for gels and dispersions, the Carreau/Yasuda model function is mostly applicable to polymers that are unlinked and unfilled. The expression for this model is

$$\frac{\eta(\gamma)-\eta_\infty}{\eta_0-\eta_\infty} = \frac{1}{(1+(\lambda\,\gamma)^{p_1})^{\frac{1-p}{p_1}}} \quad (8)$$

where λ is the relaxation time, s, γ is the shear rate, s^{-p}, p is the power-law index, dimensionless, and p_1 is the Yasuda exponent, also dimensionless (Mezger, 2006).

2.8.4. Herschel-Bulkley model

The Herschel-Bulkley model follows the expression

$$\tau = \tau_{HB} + c\,\gamma^p \quad (9)$$

where τ_{HB} is the Herschel/Bulkley yield point, $lbf/100\ ft^2$, c is the flow coefficient, $Pa.s^p$, p is the Herschel/Bulkley index, dimensionless, and γ is the shear rate, s^{-p}. This model

reduces to Ostwald/de Waele model, Eq. (5), should the yield point be non-existent or insignificant (Mezger, 2006; Ibeh, 2007).

2.8.5 Bingham model

The Bingham model equations, as well as the Herschel/Bulkley model, include a yield point. This function considers that the fluid acts as an elastic solid up until this yield point is reached. From this point on, the flow will be Newtonian-like (Ibeh, 2007). The Bingham model takes the form

$$\tau = \tau_B + \eta_B \gamma \qquad (10)$$

where τ_B is the Bingham yield point, lbf/100 ft^2, η_B is the Bingham viscosity, also called plastic viscosity (PV), cP, γ is the shear rate, s^{-1}, and τ is the shear stress, dyne/cm^2 (Mezger, 2006).

Yet, it is important to understand that the Bingham model presents certain limitations. It works well at low shear rates for shear-thinning materials only through a narrow interval of approximately one-decade of shear rate (Barnes, Hutton, & Walters, An Introduction to Rheology, 1989).

2.8.6. Exponential model

The exponential model creates a viscosity curve function using a factor c, as described in the equation

$$\eta(\gamma) = \eta_0 \, e^{-c\,\gamma} \qquad (11)$$

where η_0 is the zero-shear viscosity, cP, *e* is Euler's number and γ is the shear rate, s (Mezger, 2006).

2.9. Rotational viscometry

Rotational viscometry assists in determining the flow properties of fluids in conditions in which they present simple shearing motion. Basically, it consists of two bodies with surfaces close to each other, either with one kept in motion at constant speed while the other is maintained fixed relative to the former, or with both in movement. These conventional viscometers comprise cone and plate, parallel plate and concentric cylinder geometries, though all of them include the assumption that fluid under testing is incompressible (Collyer & Clegg, 2013).

2.9.1. Parallel plate viscometer

A parallel plate viscometer is a simple shearing flow that more easily exemplifies how the theory behind viscometers works. In this system, one plate is fixed while the other one moves at constant speed, just as presented previously in Figure 1. Here, the plate velocity is the shear rate and the stress is a component of the hydrostatic pressure (Collyer & Clegg, 2013), as the schematics in Figure 3 illustrate.

There are three attributes related to materials that can holistically determine a nonlinear fluid's characteristics: the shear stress function, σ, the first normal stress difference, N_1, and the second normal stress difference, N_2. Eq. 12, 13 and 14, respectively, describe these properties.

$$\sigma(\gamma) = \sigma_{xy} \quad (12)$$

$$N_1(\gamma) = \sigma_{xx} - \sigma_{yy} \quad (13)$$

$$N_2(\gamma) = \sigma_{yy} - \sigma_{zz} \quad (14)$$

where γ is the shear rate, σ_{xy} is the stress tensor in the xy plane, and σ_{xx}, σ_{yy} and σ_{zz} are the stress tensors along the x, y and z axis, respectively (Collyer & Clegg, 2013), as Figure 3 displays.

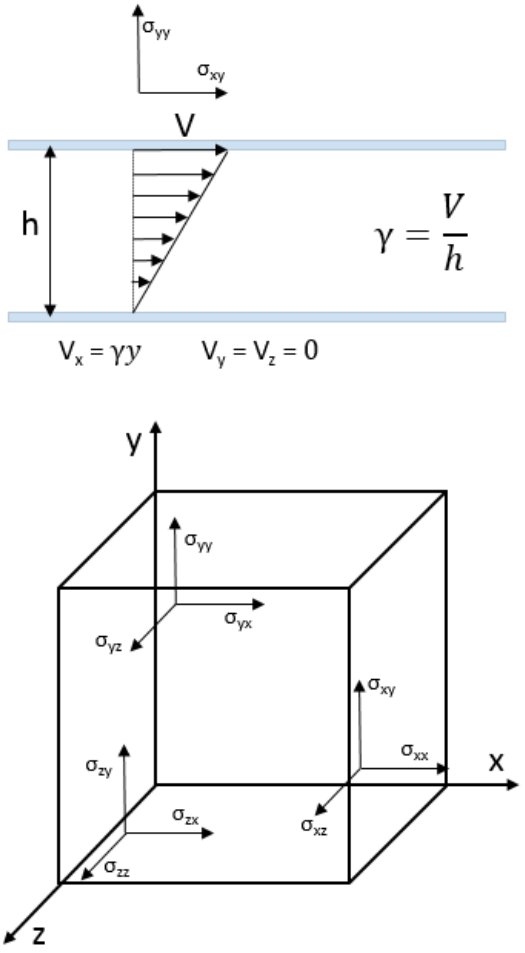

Figure 3. Simple shearing flow as presented by (Collyer & Clegg, 2013).

2.9.2. Concentric cylinder viscometer

Concentric cylinder viscometers are typically employed in measurements related to shear viscosity. In this system, the fluid in question resides in the interstice between two concentric cylinders. A schematic figure of the system is available in Figure 4.

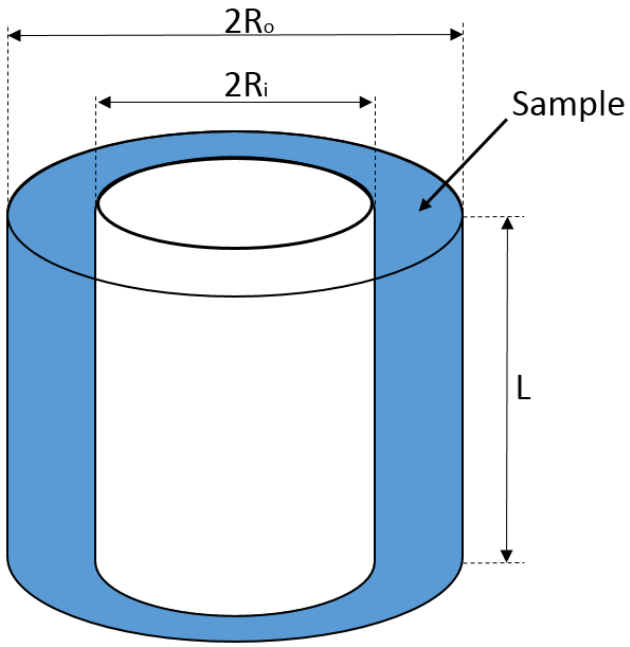

Figure 4. Collyer & Clegg (2013) schematics of the concentric cylinder viscometer. The sample is present in the shaded part.

Collyer & Clegg (2013) associated geometrical errors to concentric cylinders, including:

- the finite nature of the cylinders, which impacts negatively the assumption of an ideal flow in between both bodies;

- the neglect of the sample flow at the bottom surface of the inner cylinder, which causes shear stress.

The authors, however, suggested solutions to minimize such imperfections. For the former problem, they recommended machining the radii in such a way that would provide the same shear rate in the interstices between the inner and outer cylinder, and in between the outer cylinder and the vessel in which the system is immersed. This would increase the area where the shear stresses are measured, thus significantly reducing the effects the bottom surface causes. For the latter problem, the authors recommended the use of a hollow cavity for the inner cylinder to avoid unaccounted shear stress.

3. EQUIPMENT AND METHODOLOGY

3.1. Equipment

3.1.1. Chandler model 7600 HPHT viscometer

This study uses a high-pressure, high-temperature, concentric cylinder (i.e., coquette geometry) viscometer developed by Chandler Engineering. This equipment was designed specifically for measurements of rheological properties of drilling fluids under conditions that would be similar to those observed in oil wells, all in agreement with ISO 10414-1, 10414-2 and API 13 practices (Ametek, Chandler Engineering, 2013).

The viscometer determines the shear stress between the two cylinders (i.e., the fixed bob and the rotor) through a torsion spring and an encoder, both of which are also in agreement with the aforementioned ISO and IPO specifications. The machine obtains the viscosity by dividing the shear stress, given in dyne/cm^2, by the shear rate, given in s^{-1}. The result, as calculated, is given in Poise, defined as dyne-s/cm^2 (Ametek, Chandler Engineering, 2013).

The system's operational sample temperature interval ranges from 40 to 600°F, and its control is carried out with a programmable PID Controller, which presents a steady-state accuracy of ±1°F. The system's operational sample pressure interval ranges from atmospheric pressure to 40,000 psi. Just like the pressure control system, it uses a programmable PID controller, operating an air/liquid pump (1/400). Its accuracy is within ±500 psig (Ametek, Chandler Engineering, 2013). All the operations and measurements are executed through a computer based software.

Ametek, Chandler Engineering, (2013) provides details on the coquette geometry:

- Bob Radius (R_i): 1.7245 cm
- Rotor Radius (R_0): 1.8415 cm
- Bob Length (L): 3.805 cm
- Sample mixing via helical screw on OD of rotor with circulation ports in rotor and bob.

Ametek, Chandler Engineering, (2013) also provides the limitation on sample rheology measurements:

- Minimum Shear Stress: 5.1 dyne/cm^2
- Maximum Shear Stress: 1533 dyne/cm^2
- Minimum viscosity: 5 cP @ 600 rpm
- Maximum viscosity: 300 cP @ 300 rpm
- Shear Stress Resolution: 0.1 degree, 5.1 dyne/cm^2, 1 cP @ 300 rpm
- Shear Stress Accuracy: ± 0.50% of F.S. from 51.1 – 1533 dyne/cm^2
- Minimum Motor Speed: 1 rpm
- Minimum Shear Rate: 1.7 sec^{-1}
- Shear Rate Range: 1.7 – 1533 sec^{-1}, corresponding to 1 – 900 rpm
- Sample Gel Strength: Peak value at 3 rpm

Some other features of Chandler's model 7600 include the fact that the magnetic drive system is distant from the sample, which removes interference from ferromagnetic solids that may be suspended in the fluid, and also that the machine automatically

performs 10-10 min gel strength measurements (Ametek, Chandler Engineering, 2013). Figure 5 presents the schematics for Chandler's Model 7600 HPHT viscometer test cell.

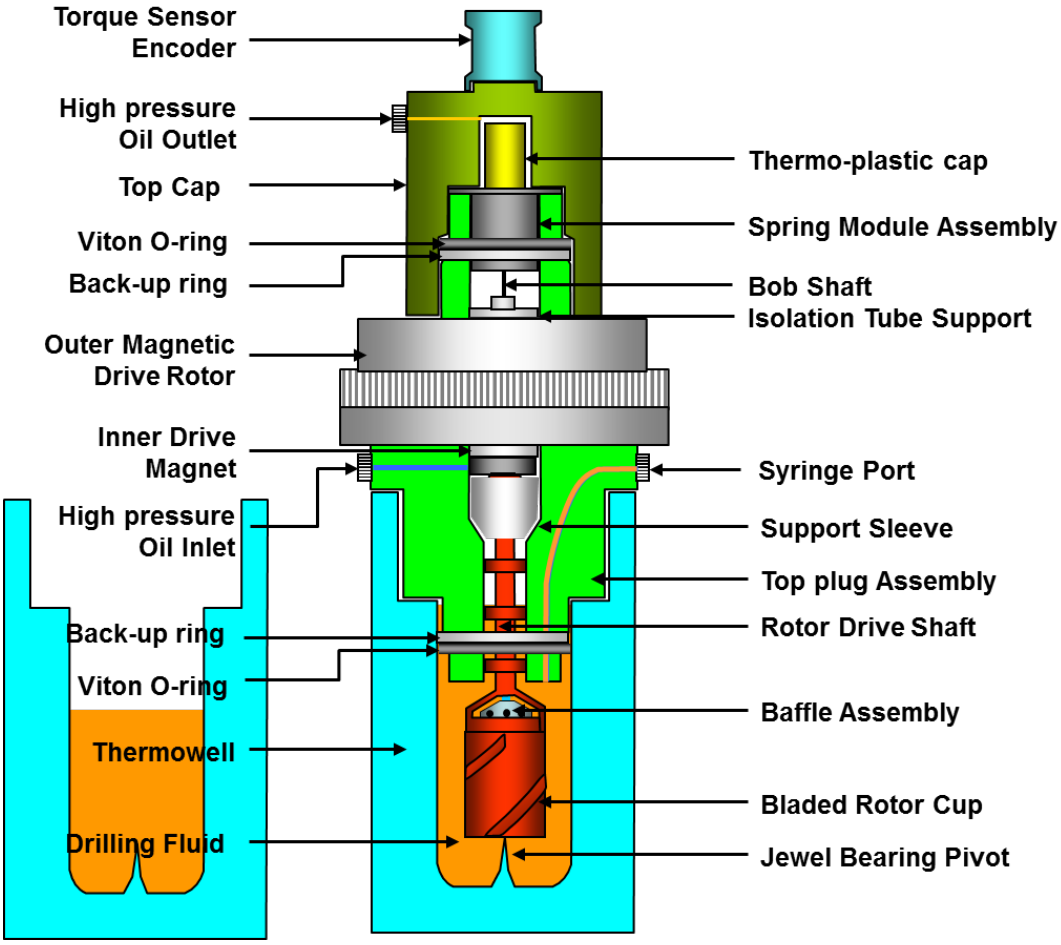

Figure 5. Chandler model 7600 HPHT viscometer test cell. Reproduced with permission of (Ibeh, 2007).

3.2. Methodology

This work uses experimental data Ibeh (2007) obtained for rheological properties of an HPHT, heavy-weight, oil-based drilling mud. This section describes the author's

procedure for preparing the samples, and designing and conducting the experiments. For additional information, please refer to Ibeh (2007).

Additionally, this section goes through the statistical and numerical methods used in analyzing the data for μ, τ, 10s GS, 10min GS, YP, n and K.

3.2.1. Design of experiment

3.2.1.1. The drilling fluid and its preparation

As previously mentioned, this study uses data Ibeh, (2007) experimentally obtained. The author used an 18.0 ppg, mineral oil-based drilling fluid with an oil/water ratio of 93/7 and electrical stability of 950. Its weighing agent was mainly barite.

Baker Hughes Drilling Fluids provided the mud samples. The company heat-aged these samples at 400ºF for 16 hours. However, solids in the sample had already considerably gravitated to the bottom of the buckets upon arrival to Texas A&M University, so mixing was necessary before carrying out the tests. Thus, the fluid was stirred with a pallet and then homogenized it with two Hamilton Beach Mixers at 70 RPM for less than 5 min. After this process, the author transferred two lab barrels to a cup and applied a uniform shear rate to this sample for 10 minutes. Finally, the author transferred a total of 200 mL of the mud to the cell of the HPHT Viscometer.

3.2.1.2. Experimental procedure

Ibeh (2007) created a factorial design for the sample analysis. In steps, the author varied the temperature from 150 to 600ºF and the pressure from 0 to 40,000 psig. Increments between intervals for the temperature were of 50ºF from 150 to 400ºF and of 25ºF from 400 to 600ºF. For pressure, increments between intervals were of 5,000 psig

for the whole interval. Additionally, for each temperature and pressure step, the HPHT Viscometer obtained readings at six different shear rates: 5.11, 10.21, 170.23, 340.46, 510.69 and 1021.38 s^{-1}. By alternating these three variables one at a time, the author obtained measurements for average μ, average τ and dial reading.

The HPHT Viscometer software also yielded results for μ, τ, 10s GS, 10min GS, YP, n and K. These, however, given the temperature and pressure, are independent of the specific shear rate the fluid is at a certain point. Thus, only temperature and pressure constitute part of the data for these properties.

3.2.2. Analysis of variance and hypothesis testing

The present study limited the data sample analyzed to the data points in the interval between 200 to 450ºF and 5,000 to 40,000 psig. This section will clarify the analysis of variance (ANOVA) and hypothesis testing used in analyzing this information.

The ANOVA F-Test in a multivariable system indicates whether each of the variables in question, and also their interactions with each other, are significant (Good & Meintrup, 2016).

In general, this study executed two variations of ANOVA. The first is an ANOVA for μ and τ with three factors, since each is a function of three different variables (temperature, pressure and shear rate). The second is a two-factor ANOVA, used for 10s GS, 10min GS, YP, n and K, as these consist in functions only of temperature and pressure.

The steps present in the ANOVA are: 5, 10, 15, 20, 25, 30, 35 and 40 ksig for pressure; 200, 250, 300, 350, 400, 425 and 450ºF for temperature; and 5.11, 10.21, 170.23, 340.46, 510.69 and 1021.38 s^{-1} for shear rate. It is worth mentioning that the latter is only applicable to μ and τ, whereas the temperature and pressure steps are applicable to all.

Due to the cumbersome nature of these ANOVA statistical calculations, especially when dealing with many steps, variables and sets of data, the author solved these computations with the aid of Wolfram Mathematica® software. The script, written in the Mathematica® language, calculated the degrees of freedom, sum of squares, mean squares, F-ratio and P-values. By comparing the latter to the significance level, 0.05 for the present work, one can determine whether one should either reject or accept the Null Hypothesis. If the P-value is below the significance level value, one may reject the Null Hypothesis, which indicates actual relevance in the evaluated term. The contrary is also true (Basso, Pesarin, Salmaso, & Solari, 2009).

3.2.3. Nonlinear regression models

This work used several numerical methods already built in Wolfram Mathematica® to fit polynomial, exponential and logarithmic models to the rheological data. Preference of one method to another was based on the value each of them yielded for the coefficient of determination, or R^2. This is done for descent and nonlinear least squares problems alike. This section briefly presents an overview of each of the numerical methods used in this work.

3.2.3.1. Newton

Newton's method is a descent method. That is, it satisfies the condition

$$F(x_{k+1}) < F(x_k) \quad (15)$$

for every step of the iterative process. Based on the assumption that the final converging value, x*, is stationary, it follows that

$$F'(x^*) = 0 \quad (16)$$

From this, as Madsen, Nielsen, & Tingleff (2004) presented, one obtains a nonlinear set of equations. Further expanding it in a Taylor expansion:

$$F'(x + h) = F'(x) + F''(x)h + O(||h||^2) \quad (17)$$

$$F'(x + h) \simeq F'(x) + F''(x)h \quad (18)$$

if $||h||$ is small enough. Thus, for Newton's method, one need only determine h_n in

$$H\, h_n = -F'(x) \quad (19)$$

where $H = -F''(x)$. Finally, assign the following iterate the value of $(x+h_n)$.

3.2.3.2. Levenberg-Marquardt

Marquardt (1963) suggested an alternative algorithm to determine the least-squares of nonlinear parameters. Essentially, it consisted in an interpolation between two methods: the Taylor series and also the gradient method. This technique bases itself in the interpolation over vicinity where the Taylor series presents a satisfactory depiction of the given model. Lourakis (2005) describes it as a mixture of the Gauss-Newton and the Steepest Descent methods. That is not without reason: as the solution is still distant from the final converging value, is takes the characteristics of the Steepest Descent,

converging slowly, but surely. Then, as it converges to the final value, it becomes the Gauss-Newton Method.

As previously mentioned, the model consists in the modification of the Gauss-Newton technique. It transforms

$$\underline{\theta}_k = \underline{\theta}_{k-1} - \underline{\eta}_{k-1}(\underline{J}_{k-1}^T \underline{J}_{k-1})^{-1} \underline{J}_{k-1}^T \underline{f}_{k-1} \quad (20)$$

into

$$\underline{\theta}_k = \underline{\theta}_{k-1} - \underline{\eta}_{k-1}(\underline{J}_{k-1}^T \underline{J}_{k-1} + \alpha_{k-1}\underline{I})^{-1} \underline{J}_{k-1}^T \underline{f}_{k-1} \quad (21)$$

where the gradient is $g \approx \underline{J}^T f$ and, by approximation, the Hessian is $H \approx \underline{J}^T J$. There is no explicit matrix inversion; instead, one solves the following expression

$$(\underline{J}_{k-1}^T \underline{J}_{k-1} + \alpha_{k-1}\underline{I})\underline{p}_{k-1} = \underline{J}_{k-1}^T \underline{f}_{k-1} \quad (22)$$

Notice that the additional term, $\alpha_{k-1}\underline{I}$, is responsible for whether the method, at a given iteration, will behave as the Gauss-Newton or the decent method (Nelles, 2013).

3.2.3.3. Conjugate gradient

The conjugate gradient method is noticeable in nonlinear optimization. The fact that it is simple and also needs very little memory, even for large-scale problems, have helped popularizing it. Comparing other methods, which may require the solving of a significantly large Hessian matrix, a computationally expensive process, can help one understand how a slower method may be preferable (Nocedal, 1996).

In summary, this method works by minimizing the expression

$$f(x) = \frac{1}{2} * x^T A_x - b^T x \quad (23)$$

At every run, the algorithm utilizes the residual, r_i, given by

$$r_i = b - Ax_i \quad (24)$$

and the previous conjugate direction, p_{i-1}, to calculate a fresh conjugate direction, p_i. Finally, the method determines a factor, α, that will minimize $f(x_i + \alpha p_i)$ (Griva, Nash, & Sofer, 2009).

3.2.3.4. NMinimize

NMinimize is a global optimization function already built in Wolfram Mathematica®. It is a numerical method with various algorithms that work by permitting the finding of the overall optimum by either decreasing or increasing the objective function. This method is extremely powerful, in the sense that it is uncommon for it to find itself wedged in local optima. Naturally, this method is computationally costly (Wolfram Mathematica, 2016).

The numerical methods for constrained global optimization programmed into the NMinimize function are Nelder-Mead, Differential Evolution, Simmulated Annealing and Random Search.

An algorithm of direct search, Nelder-Mead keeps (n+1) points for a system with n variables. In every run, the (n+1) points $x_1, x_2, \dots, x_{n+1}$ form a geometric figure, a polytope. These points of the polytope are organized so that $f(x_1) \leq f(x_2) \leq \cdots \leq f(x_{n+1})$. Then, the algorithm generates a new point, x_t, thus replacing the worst, x_{n+1}. Now there are three options: (1) in case x_t is not the new best, but it is not the new worst either, then the algorithm generates a new point to substitute what is now x_{n+1}; (2) in case x_t is the new best, the algorithm expands the polytope and calculates a new point, x_e. Should $f(x_e) \leq f(x_t)$, x_e substitutes x_{n+1}. If not, the expansion is unsuccessful and

x_t substitutes x_{n+1}; (3) finally, in case x_t is worse than the second point, the algorithm reduces the size of the polytope, defining the new point with a specific set of parameters. The process converges once the difference between the new best and old best function values and also the distance between the new best and old best points fall below the tolerances (Wolfram Mathematica, 2016).

The Differential Evolution is a probabilistic function minimizer. It retains a set of m points, m typically being much larger than the number of variables. Over each run, the method generates a new set with m points. It generates the j^{th} new point by selecting three random points, e.g. x_s, x_u and x_v, from the old set, and applying a scaling factor, s, in the following fashion

$$x_s = x_w + s(x_u - x_v) \quad (25)$$

The algorithm then obtains a new point from x_j and x_s by, with a certain probability, taking the i^{th} member from x_s and, otherwise, taking from x_j. Should $f(x_{new}) < f(x_j)$, then x_{new} substitutes x_j (Wolfram Mathematica, 2016).

Simulated Annealing is another probabilistic function minimizer. The algorithm randomly creates a new point at every run. The distance of the vicinity reduces with every iteration, and there is also tracking of the best point. If the test $f(x_{new}) \leq f(x_{best})$, the new point replaces the best. Otherwise, there is a certain probability that x_{new} will replace x (Wolfram Mathematica, 2016).

The Random Search method creates a set of random points at the beginning. The algorithm then utilizes local optimization procedures for all points from the generated set, seeking to converge to a local minimum (Wolfram Mathematica, 2016).

4. RESULTS

As previously mentioned, this work presents two different ANOVA: a three-factor ANOVA for μ and τ and a two-factor ANOVA for 10s GS, 10min GS, YP, n and K. The ANOVA execution used a significance level of 0.05. Table 2 presents a summary of the results obtained from the hypothesis testing performed with the data from each ANOVA. A detailed description of the ANOVA results is available in Appendix A.

When the Null Hypothesis applies to a term, this work disregards the effect of that term. Thus, as Table 2 shows, for μ, the combined interactive effects between pressure (P), temperature (T) and shear rate (γ) may be neglected. The Null hypothesis applied to none of the terms in τ and in YP, whereas for 10s GS, 10min GS, n and K, the combined interaction effect of P and T may be neglected.

Table 2: Summary of results obtained from hypothesis testing with the ANOVA results.

Property	Null Hypothesis Applies to
$\boldsymbol{\mu}$ (T, P, γ)	P*T*γ
τ (T, P, γ)	None
10s GS (T, P)	P*T
10min GS (T, P)	P*T
YP (T, P)	None
n (T, P)	P*T
K (T, P)	P*T

This work started by selecting the data from 200 to 450ºF and 5,000 to 40,000 psig. Table 3 presents a summary of the polynomial, exponential and logarithmic models

fit to μ, τ, 10s GS, 10min GS, YP, n and K of the drilling fluid in question. For each model, Table 3 shows, in bold, the best fitting nonlinear regression model along with its respective adjusted R^2 value. No model converged in an attempt to fit YP to an exponential model.

Table 3: Summary of the polynomial, exponential and logarithmic models fit for μ, τ, 10s GS, 10min GS, YP, n and K.

Property	Function	R^2	Nonlinear Regression Model
	Polynomial	**0.9873**	**Newton**
μ	Logarithm	0.9869	Newton
	Exponential	0.9557	NMinimize
	Polynomial	**0.9955**	**Newton**
τ	Logarithm	0.9955	NMinimize
	Exponential	0.9652	NMinimize
	Polynomial	**0.9828**	**NMinimize**
10s GS	Logarithm	0.9721	Levenberg-Marquardt
	Exponential	0.9342	NMinimize
	Polynomial	**0.9889**	**NMinimize**
10min GS	Logarithm	0.9833	Gradient
	Exponential	0.8557	NMinimize
	Polynomial	0.9009	Newton
YP	**Logarithm**	**0.9271**	**Levenberg-Marquardt**
	Exponential	-	-
	Polynomial	**0.9991**	**Newton**
n	Logarithm	0.9984	Gradient
	Exponential	0.9918	NMinimize
	Polynomial	**0.9825**	**Newton**
K	Logarithm	0.9771	Gradient
	Exponential	0.9449	Conjugate Gradient

This work further develops the analysis of the models that, for a single property, presented the highest R^2 value:

- For μ, Newton's nonlinear regression model for a polynomial function generated

$$\mu = -21609 + \frac{386.70}{P^{0.037119}} + \frac{0.00067988\ P^{1.9646}}{T^{1.4514}} + \frac{16344}{T^{0.037333}} + \frac{3.5032\ P^{0.68612}}{\gamma^{1.2339}} + \frac{8355.5}{\gamma^{0.028160}} + 47.852\ T^{0.37947}\gamma^{0.16185} \quad (26)$$

with an R^2 value of 0.9873;

- For τ, NMinimize yielded for an exponential function

$$\tau = -3538.2 + \frac{193.94}{P^{3.3241}} + \frac{2217.7}{T^{0.0091621}} + \frac{434.28\ P^{0.017800}}{T^{0.00083682}} + \frac{1451.6}{P^{0.70710}\gamma^{0.25794}} + \frac{959.40}{\gamma^{0.0011664}} + \frac{0.029754\ P^{1.4362}\gamma^{0.82585}}{T^{1.8008}} + \frac{7.3335\ \gamma^{1.0150}}{T^{0.57182}} \quad (27)$$

with an R^2 value of 0.9955;

- For 10s GS, Levenberg-Marquardt's method yielded for a polynomial function

$$10s\ GS = 7.2246 + 0.11218\ P^{0.46020} - 0.0000095055\ T^{2.2586} \quad (28)$$

with an R2 value of 0.9828;

- For 10min GS, NMinimize yielded for a logarithmic function

$$10min\ GS = 22.039 + 0.028613\ P^{0.64641} - 0.00055521\ T^{1.7550} \quad (29)$$

with an R^2 value of 0.9889;

- For YP, Levenberg-Marquardt's Method yielded for a logarithmic function

$$YP = 39.579 - \frac{0.49262\ P^{2.3659}}{T^{3.9311}} + \mathrm{Log}[P^{10.398}] + \mathrm{Log}[\frac{1}{T^{21.831}}] \quad (30)$$

with an R^2 value of 0.9271;

- For n, Newton's Method yielded for a polynomial function

$$n = -6.2857 + 6.1274\ P^{0.010002} + \frac{4.1000*10^5}{T^{2.8094}} \quad (31)$$

with an R^2 value of 0.9991;

- Finally, for K, Newton's Method yielded for a polynomial function

$$K = -7991 + 0.000010226\ P^{1.7306} + \frac{13210}{T^{0.061664}} \quad (32)$$

with an R^2 value of 0.9825.

5. DISCUSSION

As previously stated, this work started by selecting the data from 200 to 450ºF and 5,000 to 40,000 psig. Below 200ºF and 5,000 psig, Ibeh (2007) presented very little data, thus making extrapolations to low temperatures and atmospheric pressures not viable for any of the modeled properties.

The following sections will develop a detailed analysis of each of the obtained models.

5.1. Dynamic viscosity, μ

Being a function of three variables, μ presents considerable difficulties in displaying its data in a printed format. Thus, this work will analyze the μ data through different kinds of graphs: contour and 3D plots, and cross sections of the 3D graphs.

Contour plots for μ, originated from eq. 26, are available in Figure 6. They present P vs. T plots for γ values of 5.11, 10.21, 170.23, 340.46, 510.69 and 1021.38 s^{-1}. It is important to state that, in spite of the scale colors be the same for each graph, the intensity at which values change varies considerably from one plot to the next.

From Figure 6, the effects of temperature and pressure, as well as γ, over the fluid's μ are clear. As expected, for any given γ, the model indicates that increases in temperature and decreases in the pressure will considerably reduce the fluid's μ.

Increases in γ also implied drastic differences in the observations, and the μ contours demonstrate that, as one contrasts one graph to the other. First, there are vast discrepancies in the absolute values of the color scales of the μ contours, varying from

400 to 1600 cP at $5.11s^{-1}$, from 0 to 500 cP at $170.23s^{-1}$, and finally reaching 0 to 400 cP at $1021.38s^{-1}$. Thus, increases in γ significantly shorten the predicted interval for μ values of the drilling fluid analyzed. Second, the shape of the μ contours in each of the graphs also varies greatly: at $5.11s^{-1}$, they are almost linear, but slowly gravitate to a format that resembles the top part of several concentric ellipses. This happens especially at higher γ and temperature values, greater than $510.69s^{-1}$ and 300ºF, respectively, and becomes considerably pronounced at $1021.38s^{-1}$.

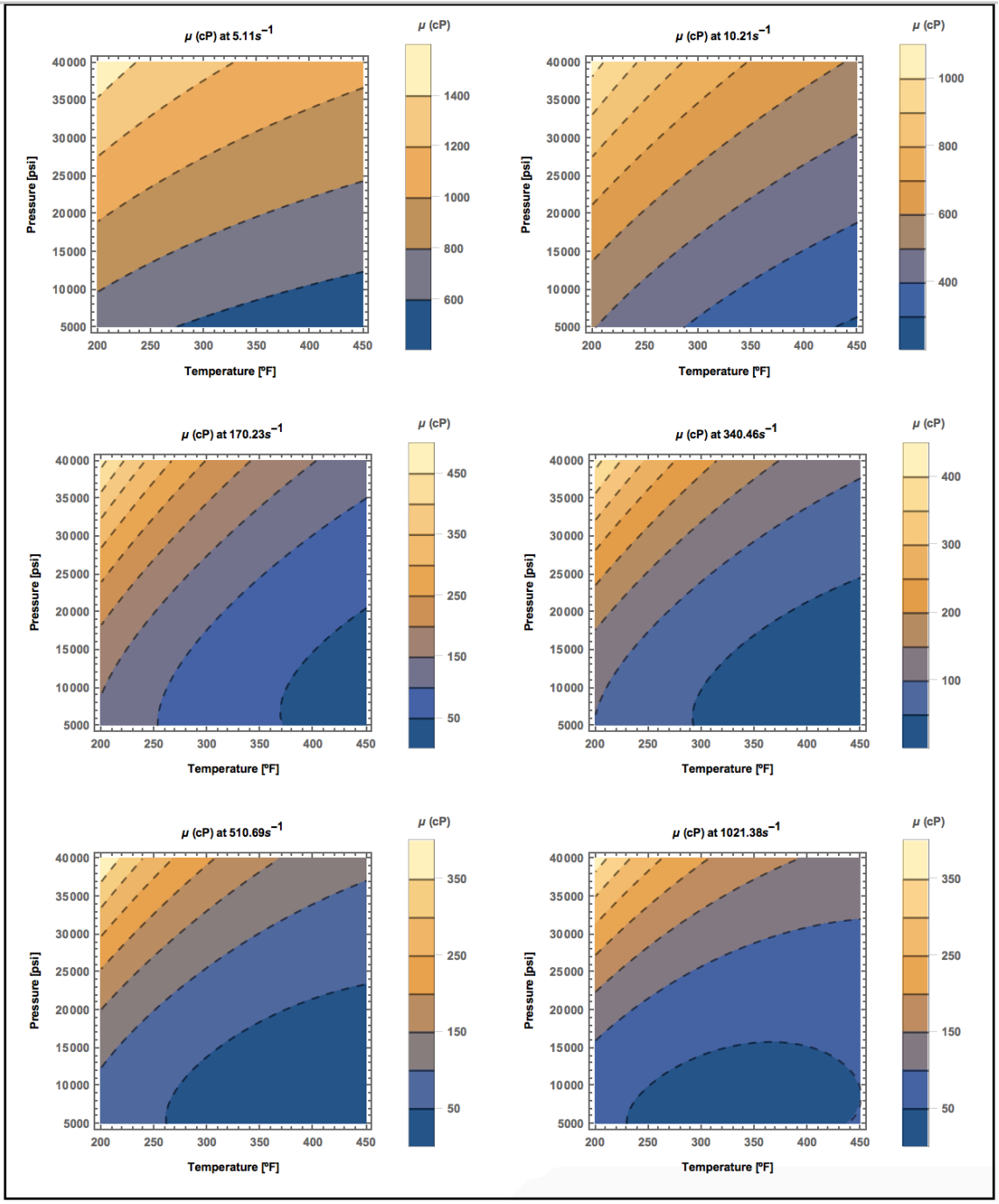

Figure 6. μ contour plots for P vs. T at γ values of 5.11, 10.21, 170.23, 340.46, 510.69 and 1021.38 s^{-1}.

This study also created 3D plots of the model-predicted surfaces for μ at given γ values, along with a scatter plot of the original data. Figure 7 displays 3D plots for 5.11, 340.46, and 1021.38 s^{-1}. Plots for all γ values samples are available in Appendix B.

Figure 7 further illustrates the positive effect in μ as pressure increases and temperature decreases. It also shows how close the μ surface from the model generally is to the data points. This description is significantly improved at higher γ (greater than 170.23s^{-1}). This is due to the fact that at low γ, i.e. barely moving (e.g. 3-6 RPM), the fluid behavior tends to approach that of gel strength.

Cross sections of all 3D graphs for μ are available in Appendix C.

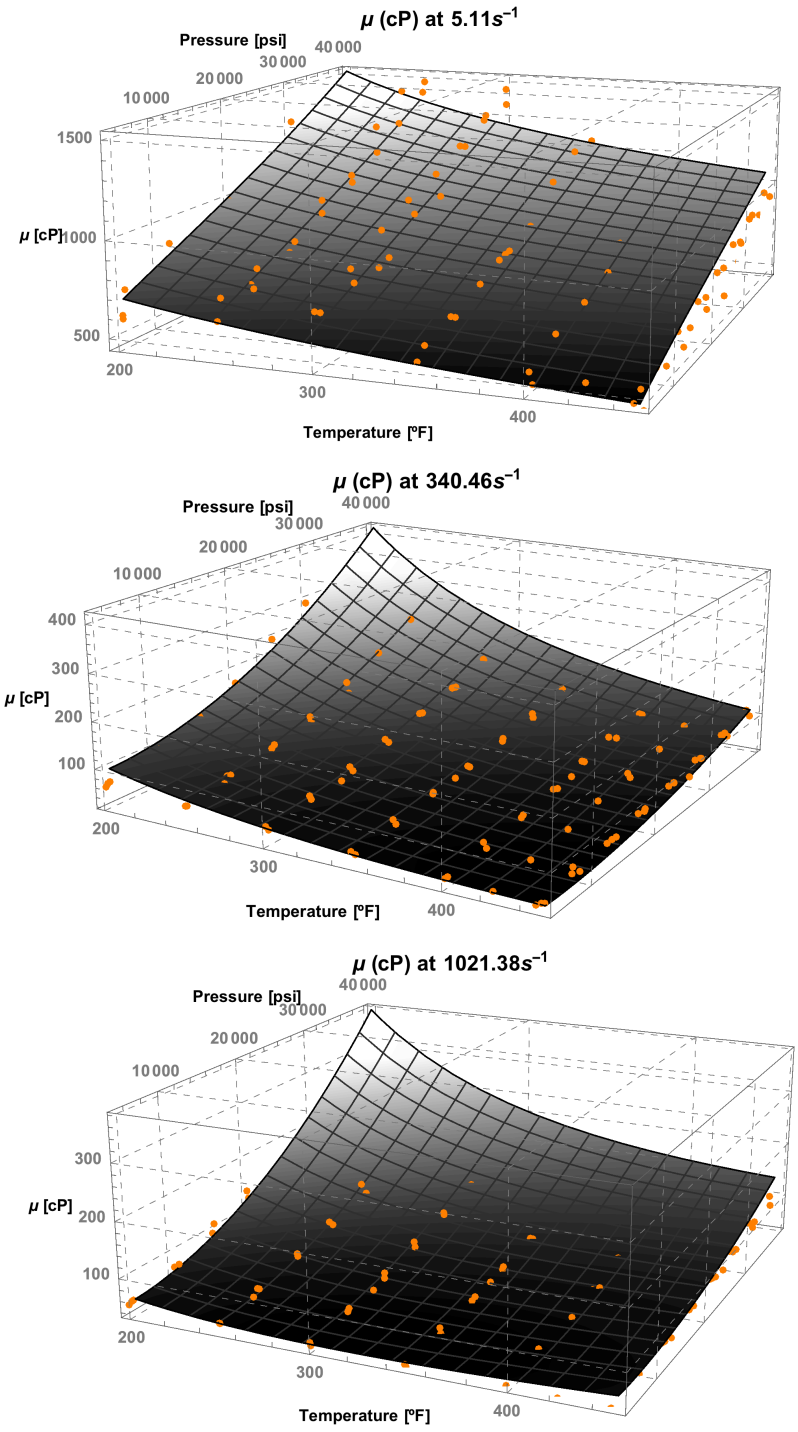

Figure 7. μ -T-P surface graphs at γ values of 5.11, 340.46, and 1021.38 s^{-1}.

5.2. Shear stress, τ

The graphic representation of τ offers the same difficulties as μ. Therefore, its data analysis and display is analogous to that of μ, also with contour and 3D plots, and cross sections of the 3D graphs.

Contour plots for τ, originated from eq. 27, are available in Figure 8. Just like those for μ, they present P vs. T plots for γ values of 5.11, 10.21, 170.23, 340.46, 510.69 and 1021.38 s^{-1}. Once again, it is important to notice that the intensity at which the scale color values change varies considerably from one plot to the next.

As expected, Figure 8 demonstrates that pressure, temperature and γ in the model expressively influence τ values. It also shows that increases in γ have a significant impact over the τ value in the drilling fluid. One can observe that the color scales in each of the graphs varies significantly: for 5.11s^{-1}, the τ interval goes from 0 to 90 dyne/cm^2; for 340.46s^{-1}, from 0 to 800 dyne/cm^2; and for 1021.38s^{-1}, from 0 to 1600 dyne/cm^2. However, unlike the results for μ, there were no significant changes in the contour formats. They approximately resemble the right-half of the parabolas with coincident zero derivative point.

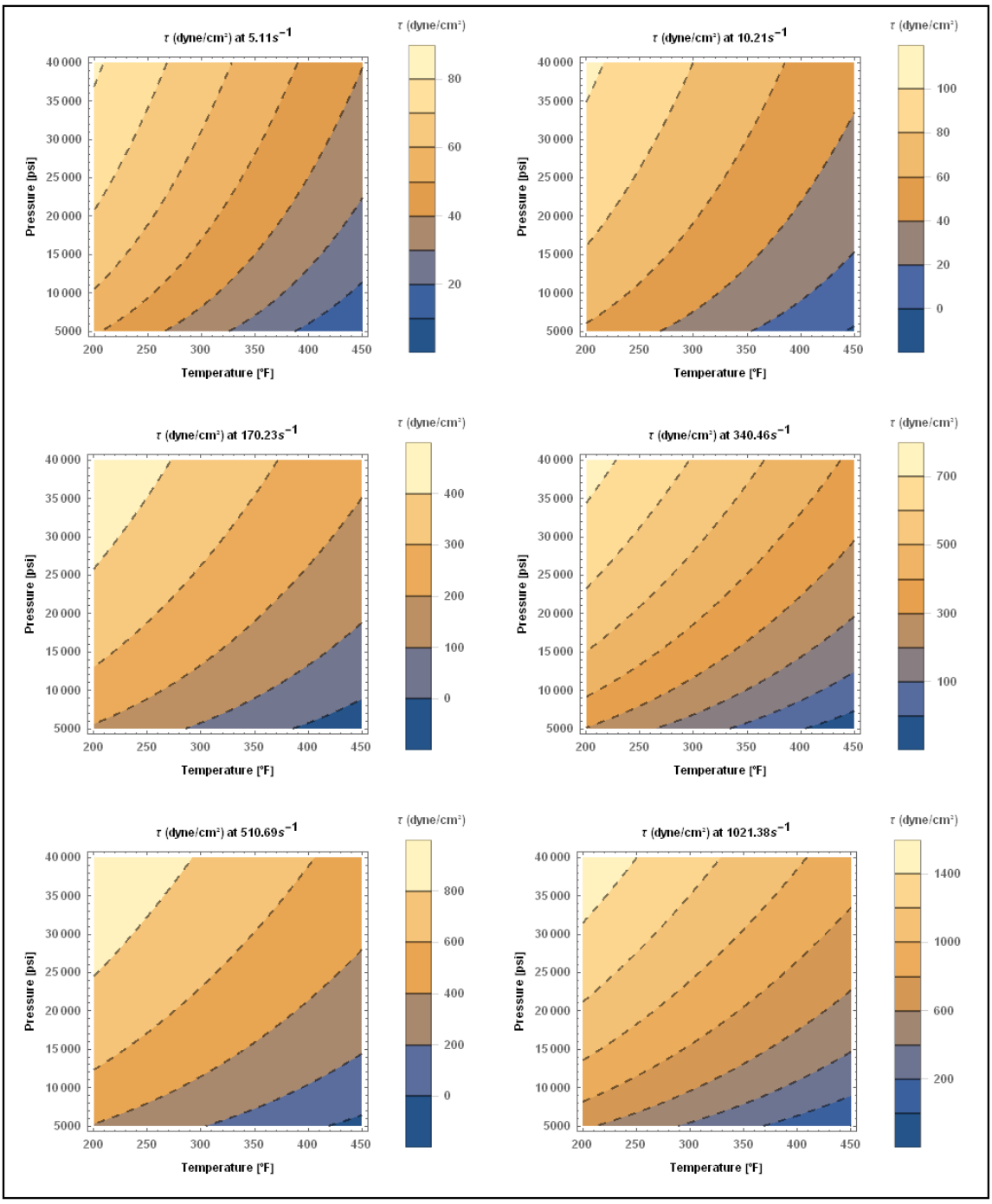

Figure 8. τ contour plots for P vs. T at γ values of 5.11, 10.21, 170.23, 340.46, 510.69 and 1021.38 s^{-1}.

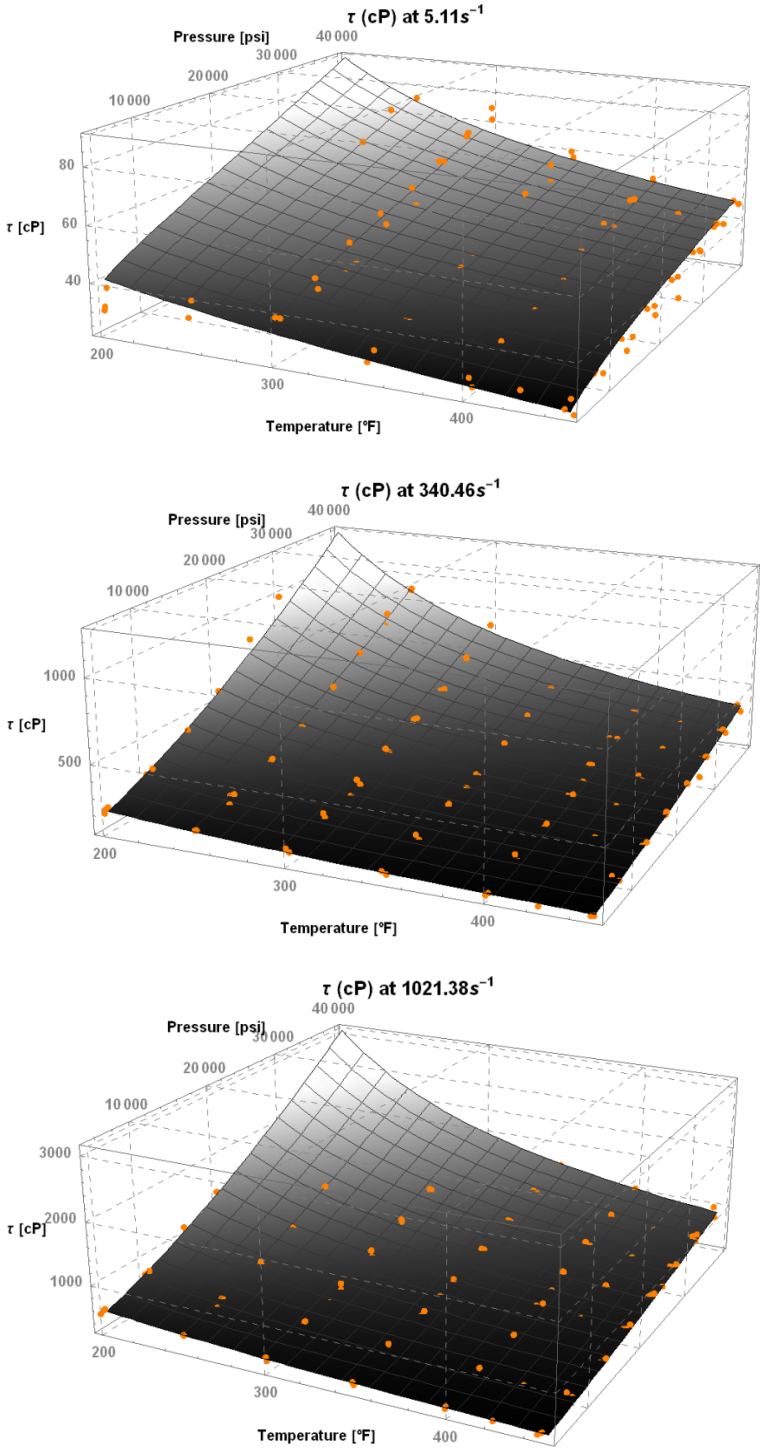

Figure 9. τ-T-P surface graphs at γ values of 5.11, 340.46, and 1021.38 s^{-1}.

The 3D graphs of the model-predicted surfaces for τ at given γ values, along with the original data points, are available in Figure 9, which displays 3D plots for 5.11, 340.46, and 1021.38 s^{-1}. Plots for all γ values samples are available in Appendix D.

Similarly to the 3D graphs for μ, one can observe that the τ surface from the model is, for the most part, very close to the data points. The model's description follows the fluid behavior with considerable accuracy at higher γ (e.g., greater than 170.23s^{-1}). One can also observe that there are distortions of the description of real behavior of the drilling fluid. This particularly occurs at very low γ, in the vicinity of 3 to 6 RPM, lower temperatures, close to 200ºF, and high pressures, beyond 20,000 psi. Naturally, this is no issue to the applicability of the model, as these conditions are not observed in real prospects. This effect at low γ values is also due to the fact that at low γ, the equivalent of 3 and 6 RPM, barely moving, for example, the fluid behavior tends to approach that of gel strength.

It is worth mentioning, as it is also clear to see from Figure 9, that the model estimates τ very closely for all other cases.

Cross sections of all 3D graphs for τ are available in Appendix E.

5.3. 10-second gel strength, 10s GS

Figure 10 displays isotherms and isobars, originated from eq. 28, along with data points for 10s GS. From the image, it is clear that the model from eq. 28 describes the drilling fluid's 10s GS closely to the data points. It also shows an inverse effect between temperature and pressure on this property: the higher the pressure, the higher the GS, and the higher the temperature, the lower the GS.

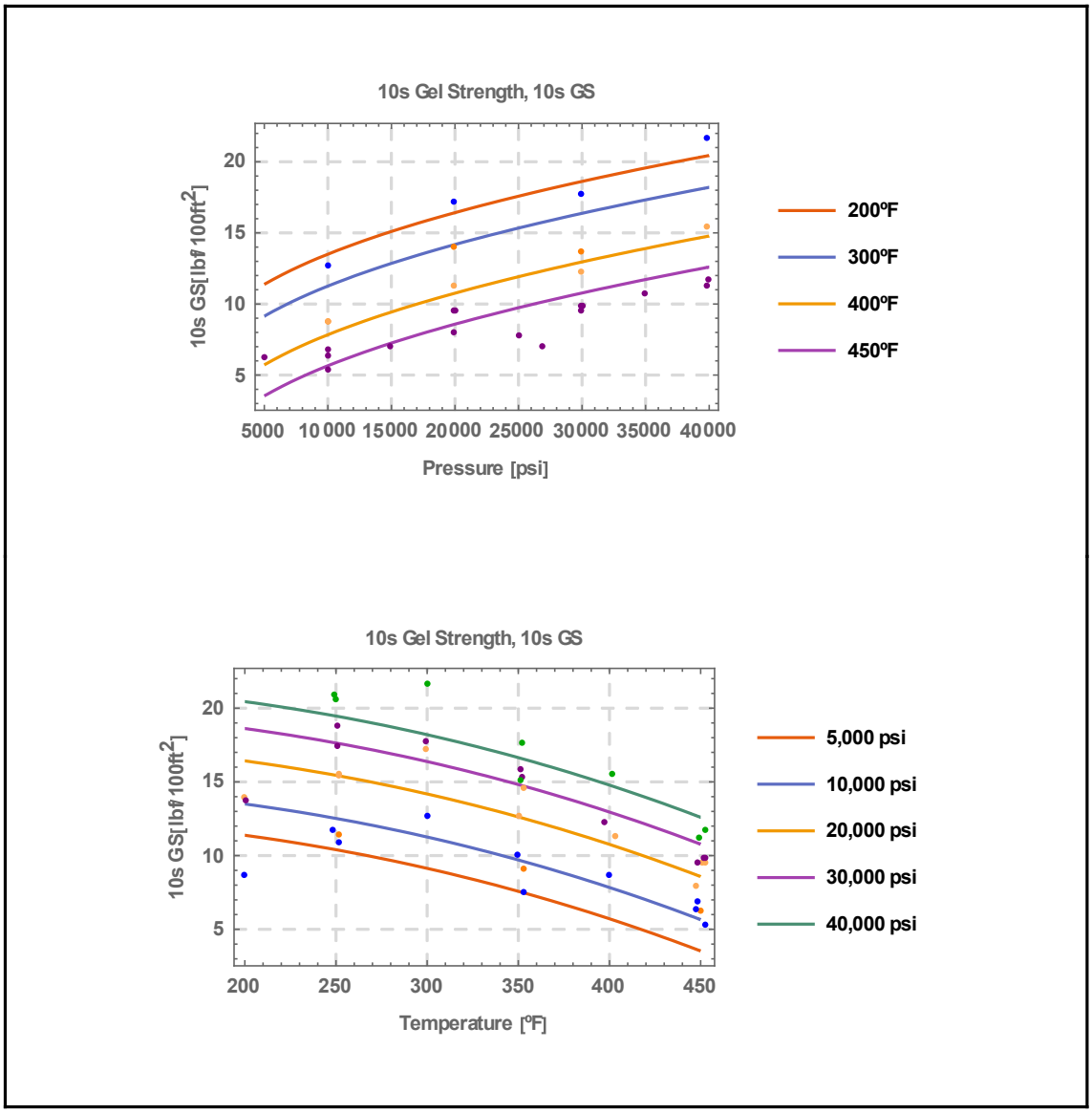

Figure 10. Isotherms and isobars for 10s GS.

5.4. 10-minute gel strength, 10min GS

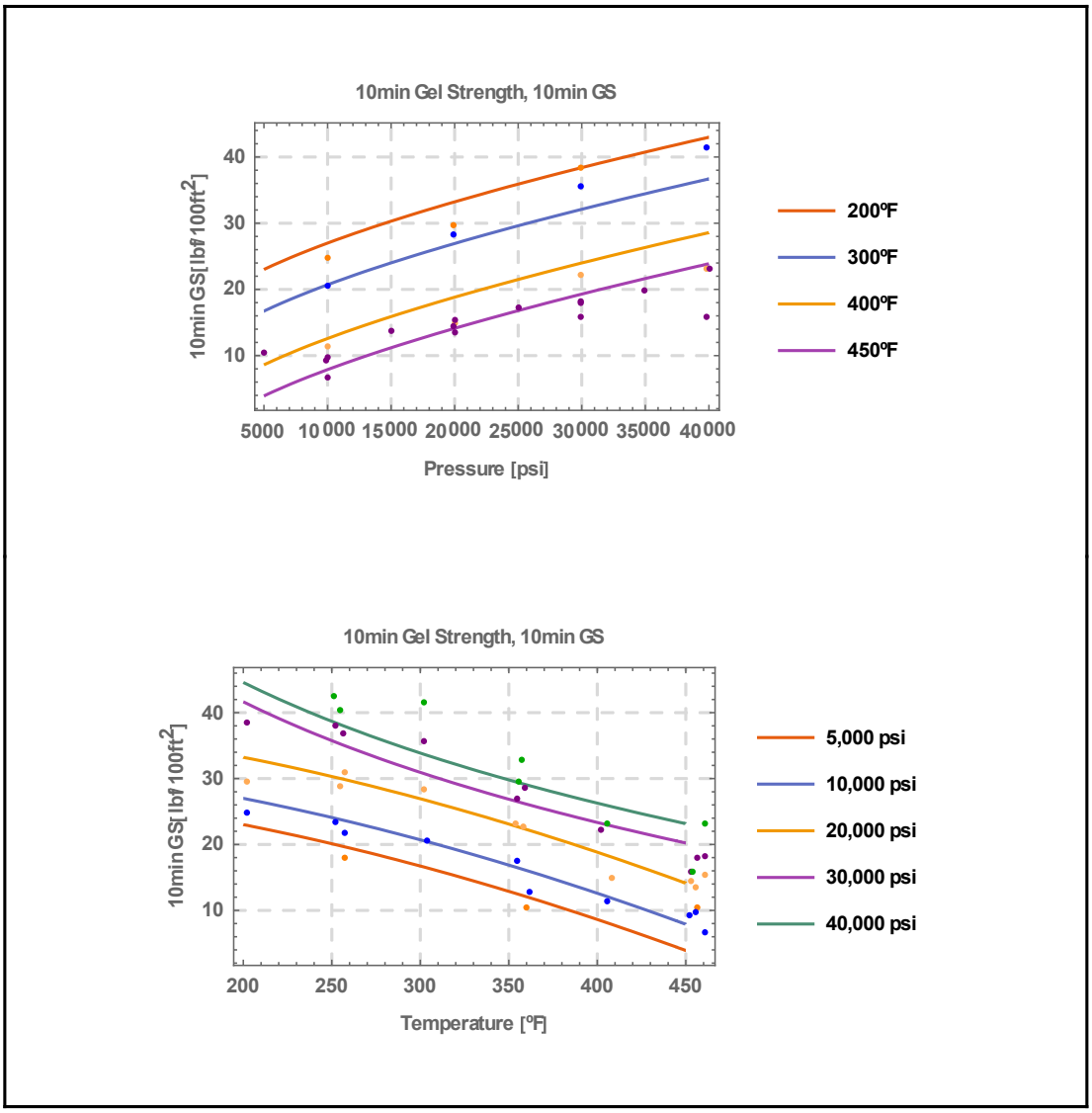

Figure 11. Isotherms and isobars for 10min GS.

Figure 11 displays isotherms and isobars, originated from eq. 29, along with data points for 10min GS. Similarly to 10s GS, the proposed model presents estimates very

close to the data points. It also demonstrates the inverse effect between pressure and temperature, increasing its value proportionally to the former and inversely proportionally to the latter.

5.5. Yield point, YP

Figure 12 displays isotherms and isobars, originated from eq. 30, along with data points for YP. With an R^2 of 0.9271, this model presents a merely acceptable estimate of the data points, though with considerably more error than the other models this research developed. Though the model follows the general direction of the data points, there is considerable scatter around the plotted curves.

The author argues that the Bingham Plastic Model, from which YP originates, actually presents a poor description of the drilling fluid analyzed. Actually, there may not even be, physically speaking, an YP for the sample. The good fits the models for n and K, which closely follow the data points, further corroborate this hypothesis: these two properties come from the Power Law Fluid Model and they are much closer to the observable fluid behavior. That is, the Power Law Fluid Model presents a better description of the sample's rheological behavior.

Figure 12 also shows that, at higher temperatures, YP values become considerably scattered around the model prediction, much more so than at lower temperatures. This may be an indicator that the drilling fluid properties are diverging from those presented at lower temperatures because of the degradation of the components present in the mud. For this same fluid in particular, Ibeh (2007) identified its failing point in the vicinity of 450ºF, which is consistent with the observations.

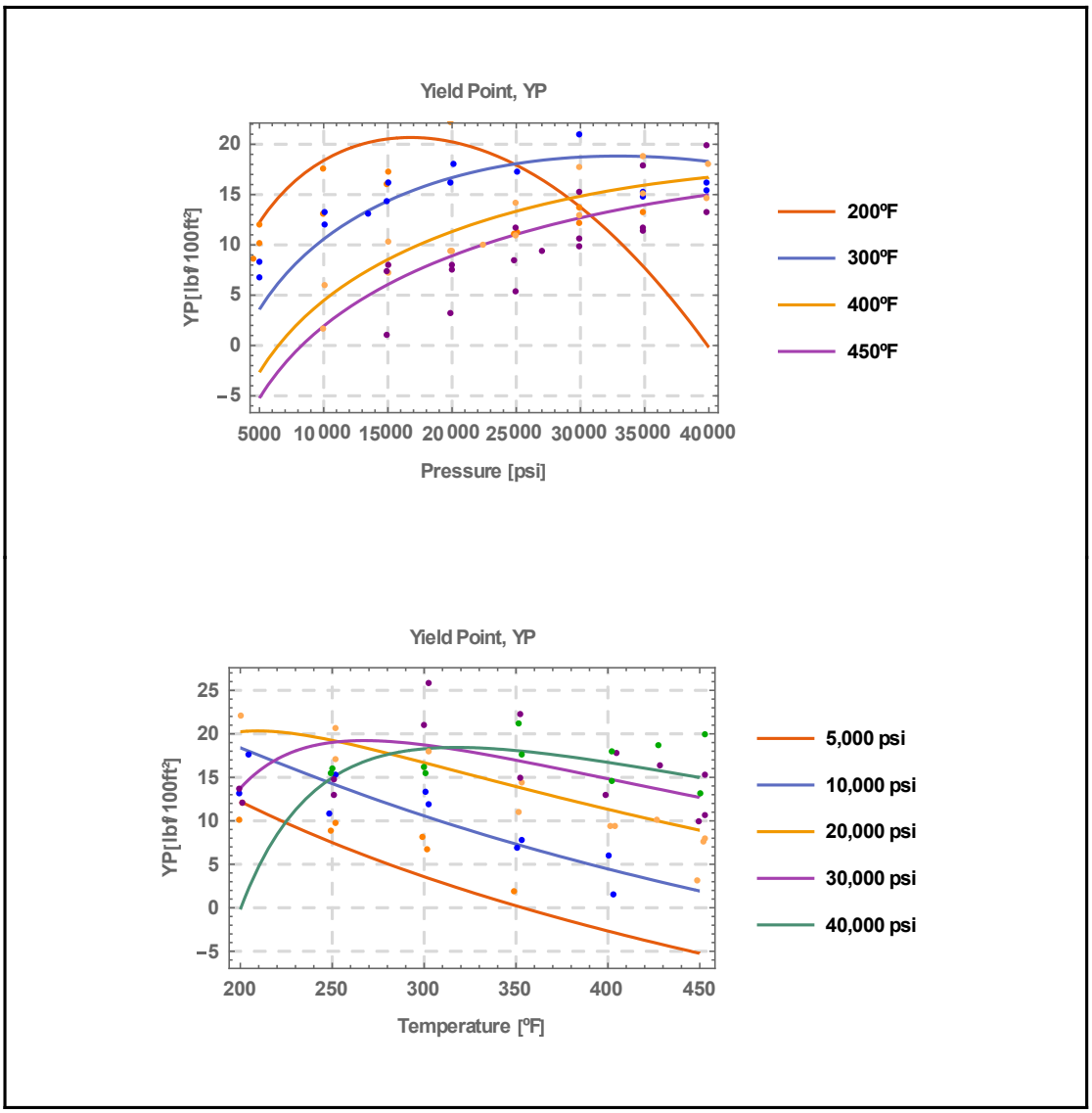

Figure 12. Isotherms and isobars for YP.

5.6. Flow behavior index, n

Figure 13 displays isotherms and isobars originated from eq. 31, along with data points for n.

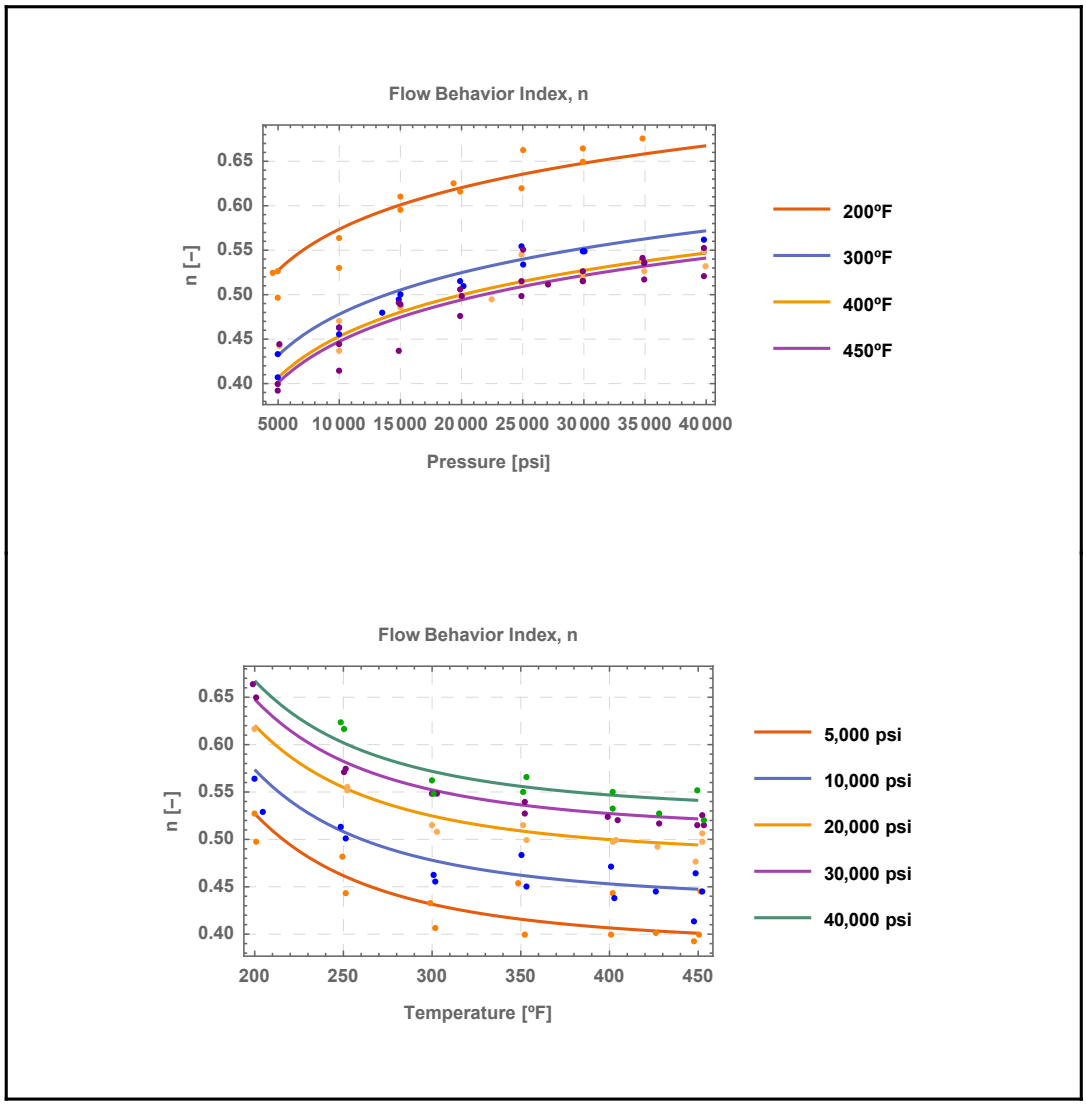

Figure 13. Isotherms and isobars for n.

The model describes that decreasing temperatures and increasing pressures will positively influence the n values, though at extremely high pressures and temperatures, the expected rate of change is weaker than that observed in milder conditions. Figure 13

demonstrates how close the model, which presents an R^2 of 0.9991, is to the observed results.

5.7. Flow consistency index, K

Figure 14 displays isotherms and isobars, originated from eq. 32, along with data points for K. These curves indicate that lower temperatures and higher pressures favor a higher value for K for the drilling fluid, depicting this very closely to the obtained data points. This model presents an R^2 of 0.9825.

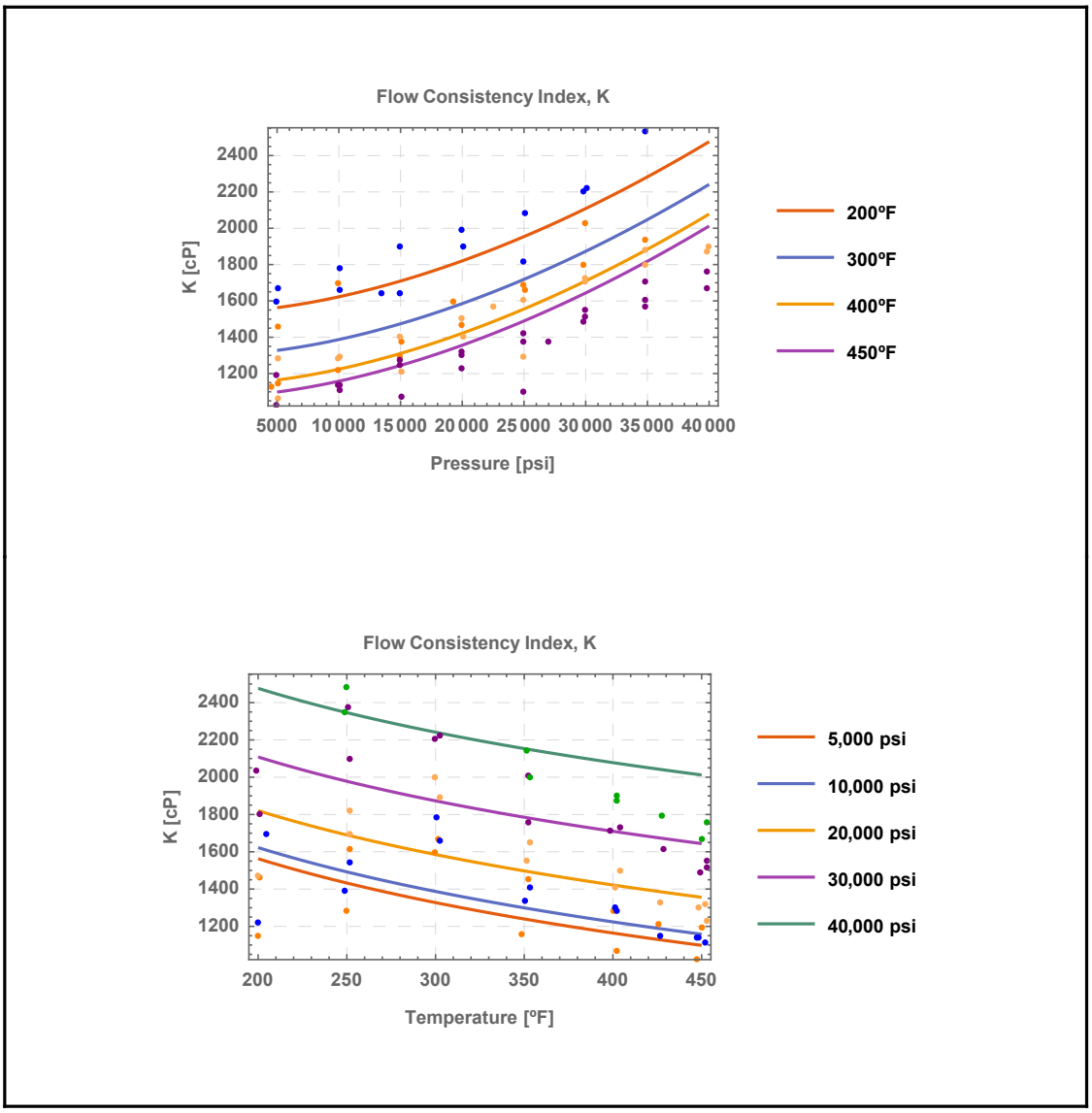

Figure 14. Isotherms and isobars for K.

5.8. Major contributions

This work presents a robust description of several rheological properties of an oil-based drilling fluid: μ, τ, 10s GS, 10min GS, YP, n and K. To the best of the author's knowledge, there are no works available in the literature that are able to consistently

describe a drilling fluid's behavior throughout pressure and temperature intervals as long as the those here developed.

Additionally, the models this work presents for μ and τ are very powerful. That is not only due to the extensive pressure and temperature intervals the models cover, but also due to the fact that the model includes the shear rate term, which may then account for different flow rates. This allows for a close estimation of the fluid's rheology over vast sections of the wellbore. Again, to the best of the author's knowledge, there are no works available in the literature that have achieved this for a drilling fluid under similar conditions.

Finally, this author understands that the use of a single drilling fluid formulation limits the applicability of the developed models. However, it is worth mentioning that this research sheds light on two facts: (1) it is indeed be possible to consistently develop a description of an oil-based drilling fluid over vast intervals of temperature, pressure and shear rate, so long as enough rheological data on the fluid is available; and (2) drilling fluids with comparable composition should behave similarly to the drilling fluid here described.

6. CONCLUSION

This work successfully obtained reliable models for rheological properties of a commercially available, dense, oil-based drilling fluid under HPHT conditions. With previously obtained data, the author developed several models for dynamic viscosity, shear stress, 10s gel strength, 10min gel strength, yield point, flow behavior index and flow consistency index that operate in vast ranges of temperature, pressure and, when applicable, shear rate: 200-450ºF, 5000-40,000 psig and 5.11-1021.38s^{-1}, respectively. All these models proved robustly consistent with laboratory data.

These results show the possibility of obtaining models that are applicable in closely describing the rheological behavior of a drilling fluid in extremely deep prospects throughout large sections of the wellbore, if not the entirety of it. Unlike other works currently available in the literature for HPHT drilling fluid rheology, these predictions would be valid even at considerably different flow conditions, as the developed models take not only pressure and temperature into consideration, but also shear rate. This may prove extremely useful in remediating certain difficulties commonly experienced in HPHT prospects, such as hydrostatic pressure prediction, wellbore cleanup, kicks, loss of drilling fluid and thermal instability of the mud.

For future studies, the author suggests: (1) analyzing other HPHT drilling fluids composed of other base fluids, including water, since costs and environmental matters are a great concern of the industry; (2) obtaining measurements of the rheology of gas-mud mixtures under HPHT conditions; (3) incorporating varying densities to a fluid's

model, since varying the mud weight is common practice in the field; (4) implementing the nonlinear numerical models in VBA coupled with an Excel® file; and (5) obtaining results in triplicates, which will increase the statistical significance of the study.

REFERENCES

Ahmad, I., Akimov, O., Bond, P., Cairns, P., Gregg, T., Heimes, T., et al. (2014). Drilling Operations in HP/HT Environment. *Offshore Technology Conference Asia* (pp. 1-14). Kuala Lumpur, Malaysia: OTC.

Amani, M. (2012). The Rheological Properties of Oil-Based Mud Under High Pressure and High Temperature Conditions. *Advances in Petroleum Exploration and Development , 3* (2), 21-30.

Amani, M., & Al-Jubouri, M. (2012). An Experimental Investigation of the The Effects of Ultra High Pressures and Temperatures on the Rheological Properties of Water-Based Drilling Fluids . *SPE/APPEA International Conference on Health, Safety, and Environment in Oil and Gas Exploration and Producti* (pp. 1-9). Perth, Australia: SPE/APPEA.

Ametek, Chandler Engineering. (2013, October). Intruction Manual. *Model 7600 HPHT Viscometer* . Broken Arrow, OK, US: Chandler Engineering Company.

Bair, S. (2007). *High Pressure Rheology for Quantitative Elastohydrodynamics.* Oxford, UK: Elsevier.

Barnes, H. A. (1997). Thixotropy - a review. *J. Non-Newtonian Fluid Mech.* , 1-33.

Barnes, H. A., Hutton, J. F., & Walters, K. (1989). *An Introduction to Rheology.* Kidlington, England: Elsevier Science.

Basso, D., Pesarin, F., Salmaso, L., & Solari, A. (2009). *Permutation Tests for Stochastic Ordering and ANOVA: Theory and Applications with R.* New York: Springer Science & Business Media.

Bird, R. B., Stewart, W. E., & Lightfoot, E. N. (2002). *Transport Phenomena.* New York, NY, USA: John Wiley & Sons, Inc.

Bland, R., Mullen, G., Gonzalez, Y., Harvey, F., & Pless, M. (2006). HP/HT Drilling Fluids Challenges. *IADC/SPE Asia Pacific Drilling Technology Conference and Exhibition* (pp. 1-11). Bangkok, Thailand: IADC/SPE.

Bourgoyne, A. T., Millheim, K. K., Chenevert, M. E., & Young, F. S. (1991). *Applied Drilling Engineering.* Richardson, TX: SPE.

British Petroleum. (2015, July 2). *BP to Settle Federal, State and Local Deepwater Horizon Claims for up to $18.7 Billion With Payments to be Spread Over 18 Years*. Retrieved from http://www.bp.com/en/global/corporate/press/press-releases/bp-to-settle-federal-state-local-deepwater-horizon-claims.html

Collyer, A. A., & Clegg, D. W. (2013). *Rheological Measurement.* Springer Science & Business Media.

Demirdal, B., & Cunha, J. C. (2009). Olefin-Based Synthetic-Drilling-Fluids Volumetric Behavior Under Downhole Conditions. *SPE Drilling and Completion* , 239-248.

El Dorry, K., Coit, A., Gutierrez, C. G., Woolums, J., & Herrington, D. (2015). Drilling Mud Cooler Opens Up New Automated Drilling Markets in Hot Hole Applications. *SPE/IADC Conference and Exhibition* (pp. 1-7). London, UK: SPE/IADC.

Elliott, D., Montilva, J., Francis, P., Reitsma, D., Shelton, J., & Roes, V. (2011). Managed Pressure Drilling Erases the Lines. *Oilfield Review* , 14-23.

Eustes, A. W. (2011). Drilling Fluids. In R. F. Mitchell, & S. Z. Miska, *Fundamentals of Drilling Engineering* (pp. 88-115). Richardson, TX: SPE.

Fox, R. W., McDonald, A. T., & Pritchard, P. J. (2004). *Introduction to Fluid Mechanics.* Hoboken, NJ, USA: John Wiley & Sons, Inc.

Good, P., & Meintrup, D. (2016). *Statistics with JMP: Hypothesis Tests, ANOVA and Regression.* Chichester, United Kingdom: John Wiley and Sons, Ltd.

Griffiths, S. K. (2012). Oil Release from Macondo Well MC252 Following the Deepwater. *Environmental Science and Technology* , 5616-5622.

Griva, I., Nash, S. G., & Sofer, A. (2009). *Linear and Nonlinear Optimization: Second Edition.* Philadelphia, PA: SIAM.

Ibeh, C. S. (2007, December). Investigation on the Effects of Ultra-High Pressure and Temperature on the Rheological Properties of Oil-Based Drilling Fluids. *Master of Science Thesis, Texas A&M* . College Station, TX, USA: Texas A&M University.

International Association of Drilling Contractors. (2005). *IADC Well Classification System for Underbalanced Operations and Managed Pressure Drilling* . IADC.

Kaufman, L. (2010, April 23). *Search Ends for Missing Oil Rig Workers*. Retrieved from The New York Times: http://www.nytimes.com/2010/04/24/us/24spill.html?hpw&_r=0

Lee, J., & Shadravan, A. (2012). Rheological Properties of Invert Emulsion Drilling Fluid under Extreme HPHT Conditions. *IADC/SPE Drilling Conference and Exhibition* (pp. 1-9). San Diego, USA: IADC/SPE.

Lourakis, M. I. (2005). *A Brief Description of the Levenberg-Marquardt Algorithm Implemented by levmar.* Heraklion, Greece: Foundation for Research and Technology - Hellas (FORTH).

Møller, P. C., Mewis, J., & Bonn, D. (2006). Yield stress and thixotropy: on the difficulty of measuring yield stress in practice. *The Royal Society of Chemistry* , 274-283.

Madsen, K., Nielsen, H. B., & Tingleff, O. (2004). *Methods for Non-Linear Least Squares Problems.* Lyngby, Denmark: DTU.

Mahmood, A., Al-Jubouri, M., & Shadravan, A. (2012). Comparative Study of Using Oil-Based Mud Versus Water-Based Mud in HPHT Fields. *Advances in Petroleum Exploration and Development* , 18-27.

Malkin, A. Y., & Isayev, A. I. (2006). *Rheology - Concepts, Methods & Applications.* Toronto, Canada: ChemTec Publishing.

Marquardt, D. W. (1963). An Algorithm for Least-Squares Estimation of Nonlinear Parameters. *J. Soc. Indust. Appl. Math.* , 431-441.

Mewis, J., & Wagner, N. J. (2012). *Colloidal Suspension Rheology.* Cambridge, UK: Cambridge University press.

Mezger, T. G. (2006). *The Rheology Handbook: For users of rotational and ocillatory rheometers.* Hannover, Germany: Coatings Compendia.

Mohanty, A. K. (2006). *Fluid Mechanics.* New Delhi, India: Prentice-Hall of India.

Nelles, O. (2013). *Nonlinear System Identification: From Classical Approaches to Neural Networks and Fuzzy Models.* Berlin, Germany: Springer Science & Business Media.

Nocedal, J. (1996). Conjugate Gradient Methods and Nonlinear Optimization. In L. M. Adams, & J. L. Nazareth, *Linear and Nonlinear Conjugate Gradient-related Methods* (pp. 9-23). Philadelphia, PA: SIAM.

Ostroot, K., Shayegi, S., Lewis, D., & Lovorn, R. (2007). Comparison of Under-balanced and Managed-Pressure Drilling Techniques. *AADE National Technical Conference and Exhibition* (pp. 1-10). Houston, USA: American Association of Drilling Engineers.

Patel, H. N., Bruton, J. W., & Buchanan, W. B. (2015). Systematic Technology Qualification for HPHT Subsea BOP Stack Equipment and System to Improve Safety, Reliability, and Availability. *Offshore Technology Conference* (pp. 1-12). Houston, USA: OTC.

Proehl, T., & Sabins, F. (2006). *DeepStar CTR 7501 - Drilling and Completion Gaps for HPHT Wells in Deep Water Final Report.* Sugar Land, TX, USA.

Ragab, A.-R., & Bayoumi, S. E. (1998). *Engineering Solid Mechanics: Fundamentals and Applications.* Boca Raton, FL, USA: CRC Press.

Rehm, B., Schubert, J., Haghshenas, A., Paknejad, A. S., & Hughes, J. (2008). *Managed Pressure Drilling.* Houston, TX, USA: Gulf Publishing Company.

Santos, H., Leuchtenberg, C., & Sara, S. (2003). Micro-Flux Control: The Next Generation in Drilling Process for Ultra-deepwater. *Offshore Technology Conference* (pp. 1-10). Houston, USA: OTC.

Savins, J. G., & Roper, W. F. (1954). A Direct-indicating Viscometer for Drilling Fluids. *South-western District, Division of Production* (pp. 7-22). Houston: American Petroleum Institute.

Shadravan, A., & Amani, M. (2012). HPHT 101 - What Every Engineer or Geoscientist Should Know about High Pressure High Temperature Wells. *SPE Kuwait International Petroleum Conference and Exhibition* (pp. 1-27). Kuwait City, Kuwait: Society of Petroleum Engineers.

Shrivastav, P. (2012). An Integrated Approach Towards Well Control For a HPHT Well. *Offshore Technology Conference* (pp. 1-6). Houston, TX, USA: OTC.

Skogdalen, J. E., Utne, I. B., & Vinnem, J. E. (2011). Developing safety indicators for preventing offshore oil and gas deepwater drilling blowouts. *Safety Science* , 11-87-1199.

White, F. M. (2006). *Viscous Fluid Flow.* New York, NY, USA: McGraw-Hill.

Wolfram Mathematica. (2016, May). *Numerical Nonlinear Global Optimization*. Retrieved from Wolfram - Computation Meets Knowledge: http://reference.wolfram.com/language/tutorial/ConstrainedOptimizationGlobalNumerical.html#217856200

Zamora, M., Roy, S., Slater, K., & Troncoso, J. (2013). Study on the Volumetric Behavior of Base Oils, Brines, and Drilling Fluids Under Extreme Temperatures

and Pressures. *SPE Annual Technical Conference and Exhibition* (pp. 278-288). San Antonio, USA: SPE.

Zhou, H., Deville, J. P., & Davis, C. L. (2015). Novel High Density Brine-Based Drill-In Fluids Significantly Increased Temperature Limit for HP/HT Applications . *SPE/IADC Drilling Conference and Exhibition* (pp. 1-13). London, United Kingdom: SPE/IADC.

APPENDIX A

Using Mathematica®, the author performed ANOVA analyses.

The ANOVA for dynamic viscosity (μ) is available below.

	DF	SumOfSq	MeanSq	FRatio	PValue
pressure	6	2.80927×10^{6}	468212.	528.057	8.53985×10^{-160}
temperature	7	4.97782×10^{6}	711118.	802.01	7.62302×10^{-195}
shearrate	5	5.60256×10^{7}	1.12051×10^{7}	12637.3	$9.15140337177661\times10^{-357}$
pressure temperature	41	526851.	12850.	14.4925	7.19441×10^{-51}
pressure shearrate	30	1.35479×10^{6}	45159.7	50.9318	7.82253×10^{-102}
shearrate temperature	35	2.20951×10^{6}	63128.8	71.1977	2.01369×10^{-127}
pressure shearrate temperature	197	68380.9	347.111	0.391478	1.
Error	311	275754.	886.669		
Total	632	6.8248×10^{7}			

The ANOVA for shear stress (τ) is available below.

	DF	SumOfSq	MeanSq	FRatio	PValue
pressure	6	3.1705×10^{6}	528417.	489.893	3.33336×10^{-155}
temperature	7	6.09461×10^{6}	870658.	807.183	2.958×10^{-195}
γ	5	3.7451×10^{7}	7.4902×10^{6}	6944.13	$1.330435266443103\times10^{-316}$
pressure temperature	41	751147.	18320.7	16.985	1.1666×10^{-57}
pressure γ	30	3.0325×10^{6}	101083.	93.7138	4.22411×10^{-137}
temperature γ	35	5.72977×10^{6}	163708.	151.773	5.23324×10^{-174}
pressure temperature γ	197	1.15539×10^{6}	5864.92	5.43734	3.30617×10^{-40}
Error	311	335456.	1078.64		
Total	632	5.77204×10^{7}			

The ANOVA for the 10-second gel strength (10s GS) is available below.

	DF	SumOfSq	MeanSq	FRatio	PValue
pressure	5	489.246	97.8492	96.6997	7.23787×10^{-11}
temperature	7	343.597	49.0853	48.5086	3.52949×10^{-9}
pressure temperature	22	32.2643	1.46656	1.44933	0.232081
Error	15	15.1783	1.01189		
Total	49	880.286			

The ANOVA for the 10-minute gel strength (10min GS) is available next.

	DF	SumOfSq	MeanSq	FRatio	PValue
pressure	5	2498.57	499.713	117.803	1.72712×10^{-11}
temperature	7	1815.04	259.291	61.1256	6.78589×10^{-10}
pressure temperature	22	163.506	7.4321	1.75205	0.133253
Error	15	63.629	4.24193		
Total	49	4540.74			

The ANOVA for the yield point (YP) is available below.

	DF	SumOfSq	MeanSq	FRatio	PValue
pressure	6	505.45	84.2417	5.62131	0.000184103
temperature	7	1042.66	148.951	9.93925	1.52227×10^{-7}
pressure temperature	36	1295.24	35.9789	2.40081	0.00253125
Error	47	704.348	14.9861		
Total	96	3547.69			

The ANOVA for the fluid behavior index (n) is available below.

	DF	SumOfSq	MeanSq	FRatio	PValue
pressure	6	0.148928	0.0248214	80.5084	7.50848×10^{-25}
temperature	7	0.212285	0.0303264	98.364	4.60066×10^{-28}
pressure temperature	41	0.0054778	0.000133605	0.433348	0.996829
Error	53	0.0163403	0.000308308		
Total	107	0.383031			

The ANOVA for the fluid consistency index (K) is available below.

	DF	SumOfSq	MeanSq	FRatio	PValue
pressure	6	6.63859×10^{6}	1.10643×10^{6}	67.8721	4.12472×10^{-23}
temperature	7	8.3972×10^{6}	1.1996×10^{6}	73.5874	5.06083×10^{-25}
pressure temperature	41	485828.	11849.5	0.726884	0.85468
Error	53	863991.	16301.7		
Total	107	1.63856×10^{7}			

APPENDIX B

3D graphs for dynamic viscosity

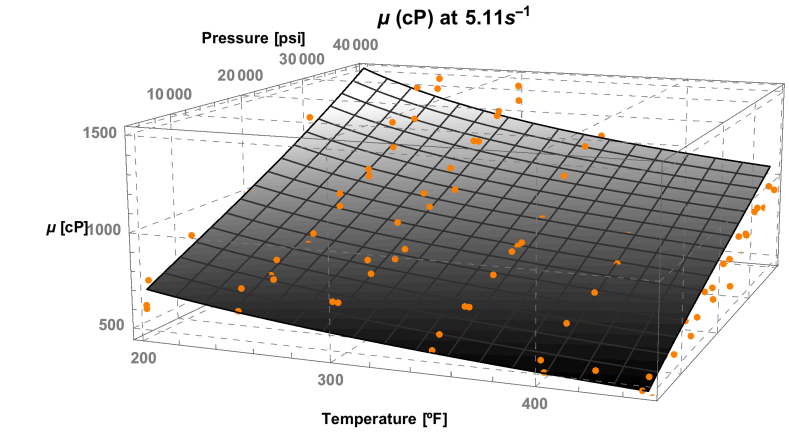

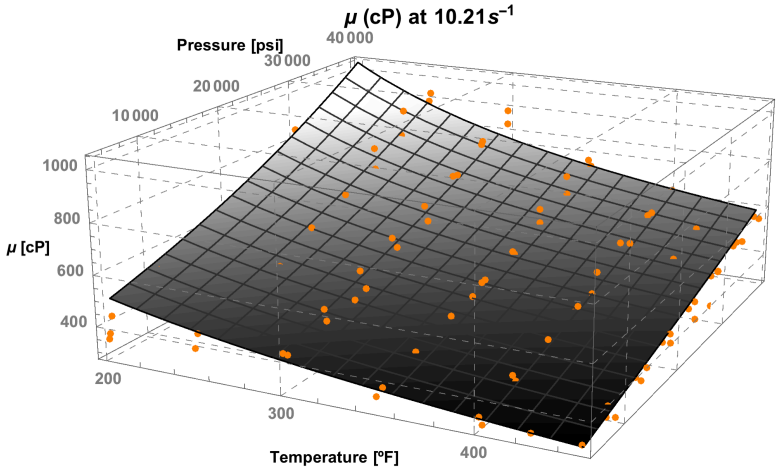

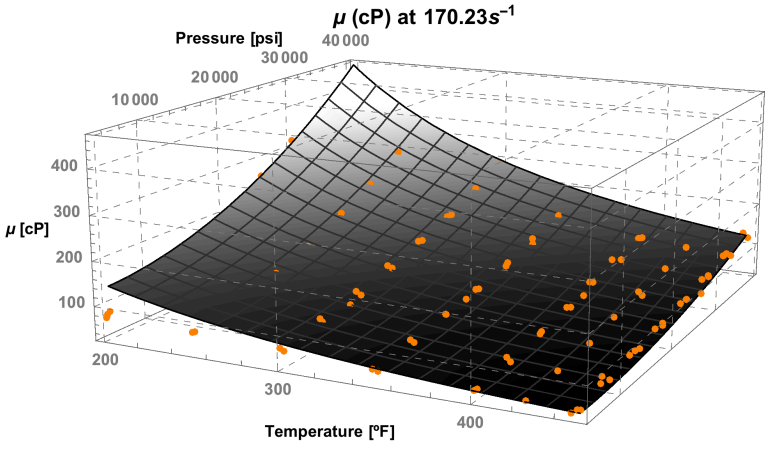

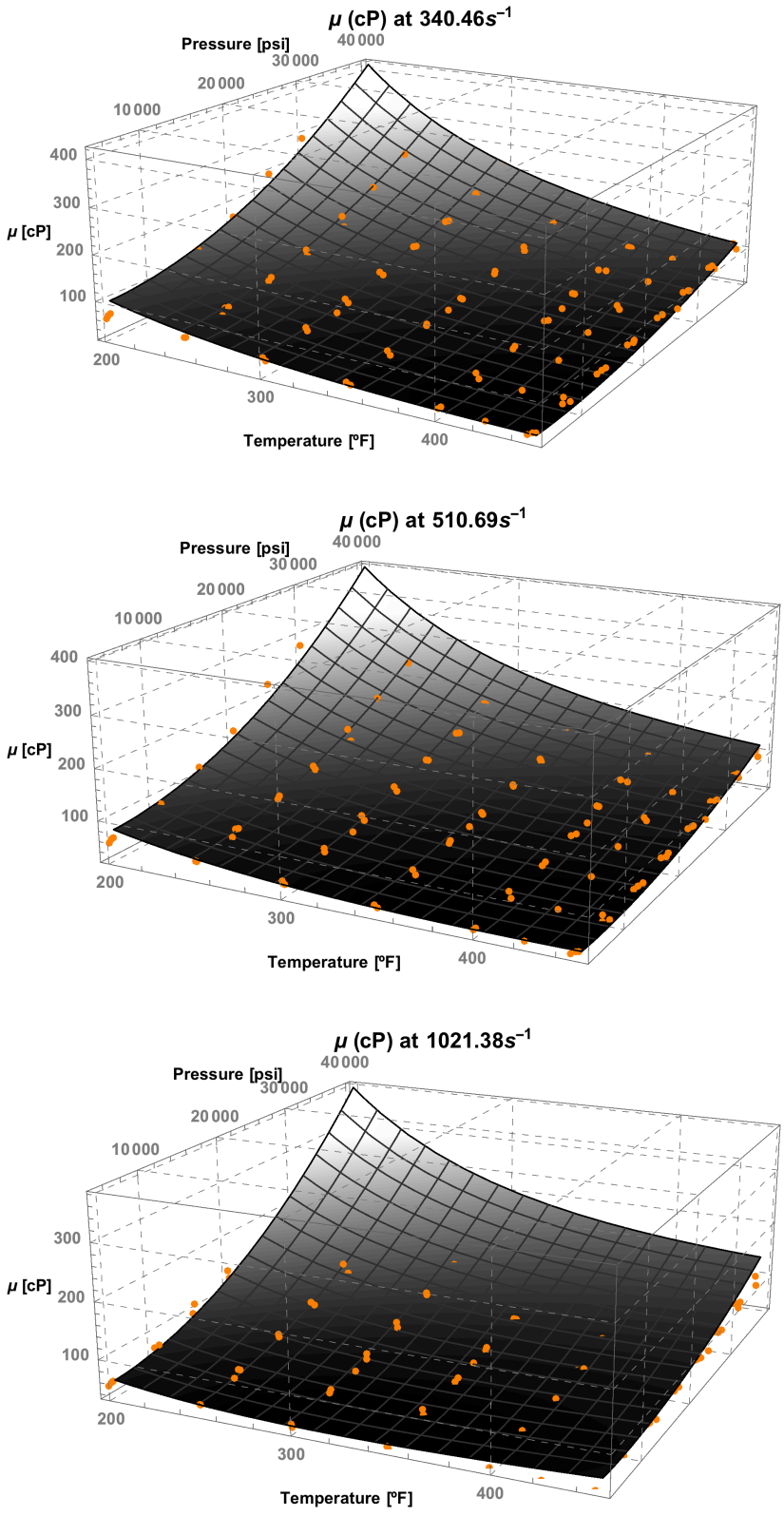
μ (cP) at 340.46s⁻¹
Pressure [psi]
40 000
30 000
20 000
10 000
400
300
200
100
μ [cP]
200
300
400
Temperature [ºF]
μ (cP) at 510.69s⁻¹
Pressure [psi]
40 000
30 000
20 000
10 000
400
300
200
100
μ [cP]
200
300
400
Temperature [ºF]
μ (cP) at 1021.38s⁻¹
Pressure [psi]
40 000
30 000
20 000
10 000
300
200
100
μ [cP]
200
300
400
Temperature [ºF]

APPENDIX C

Cross sections of 3D graphs for μ.

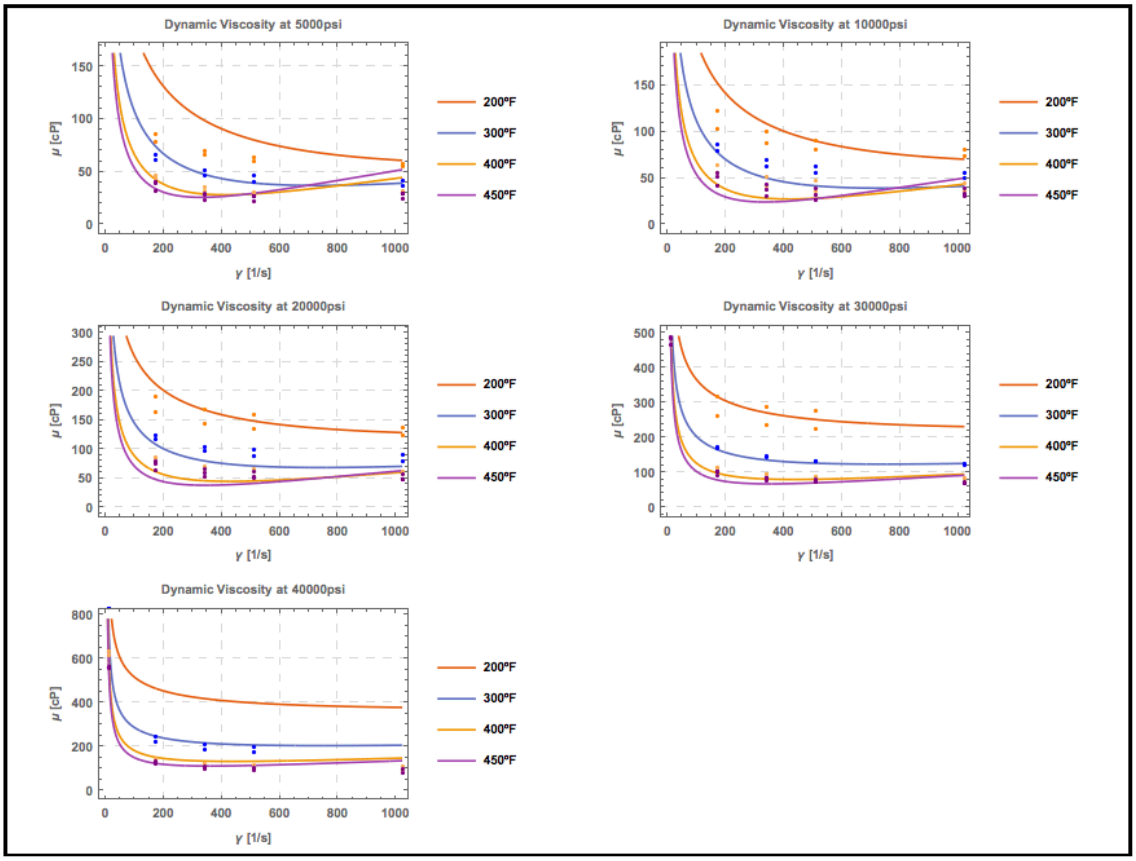

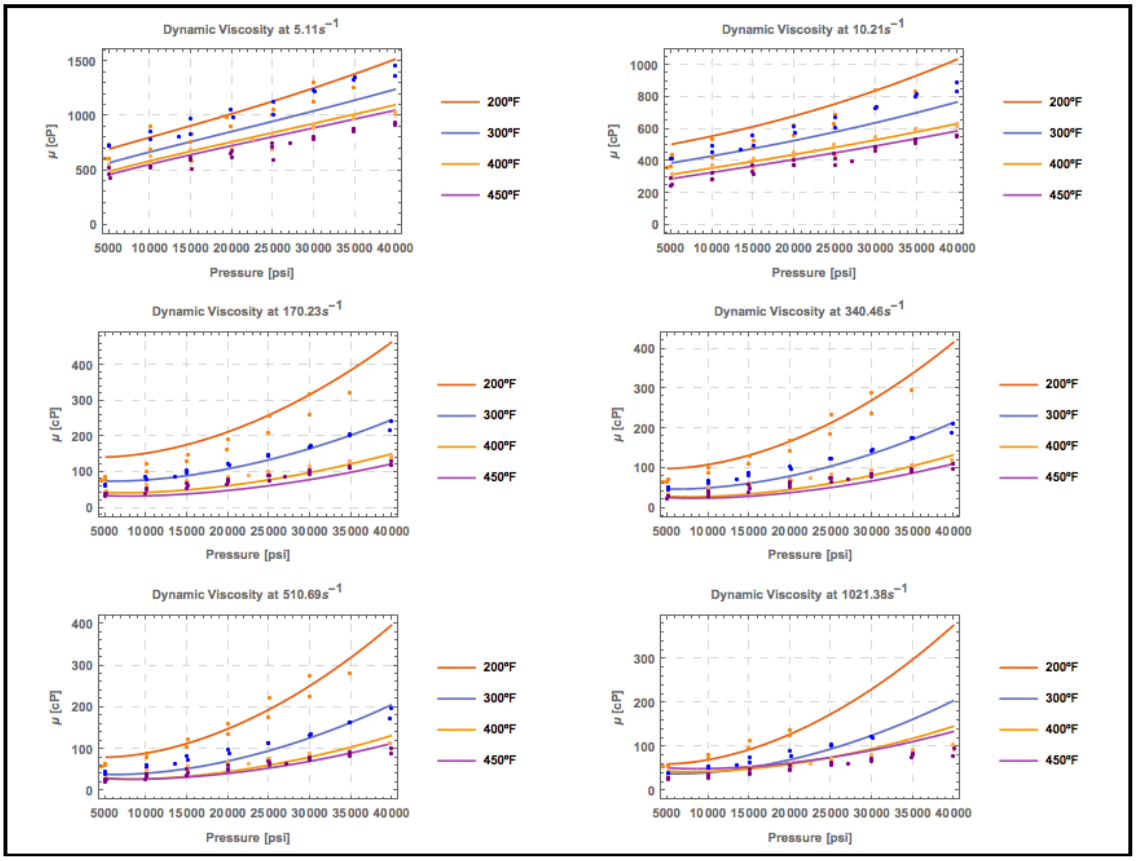
Dynamic Viscosity at 5.11s^-1
Dynamic Viscosity at 10.21s^-1
Dynamic Viscosity at 170.23s^-1
Dynamic Viscosity at 340.46s^-1
Dynamic Viscosity at 510.69s^-1
Dynamic Viscosity at 1021.38s^-1
μ [cP]
Pressure [psi]
200°F
300°F
400°F
450°F

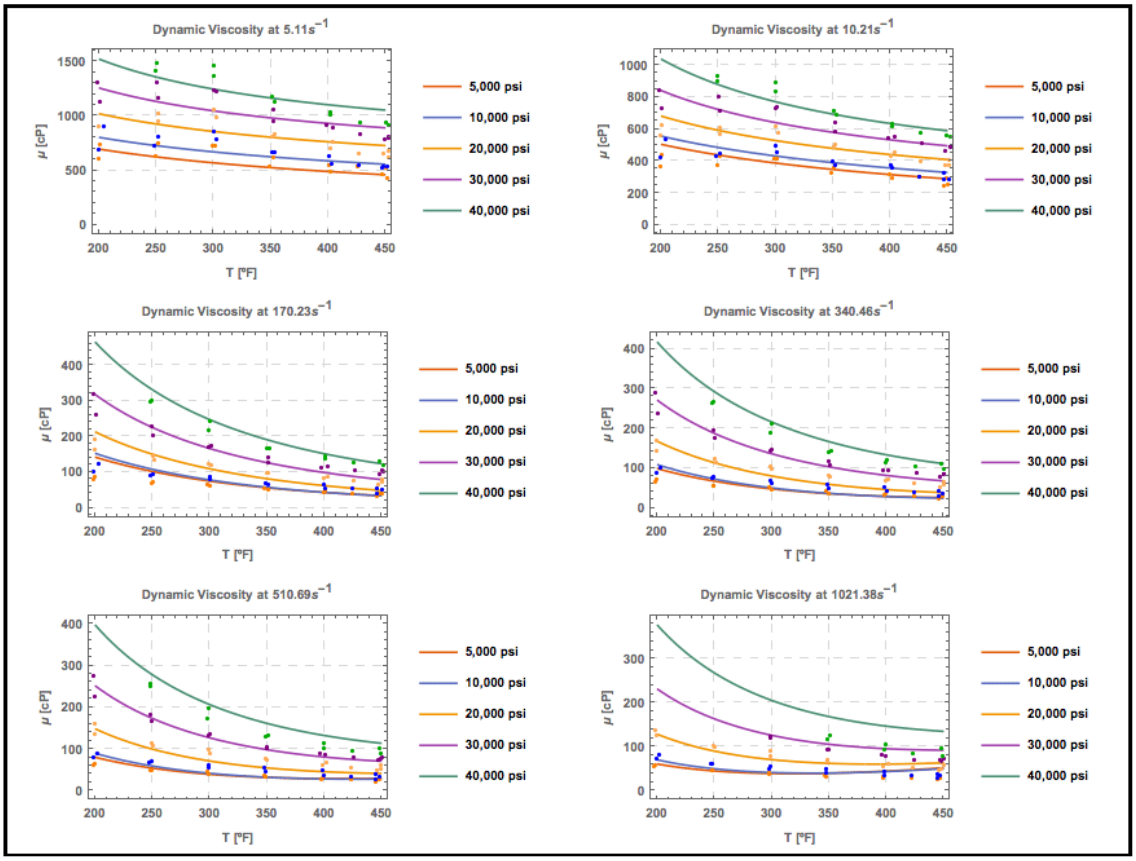
Dynamic Viscosity at 5.11s^{-1}
Dynamic Viscosity at 10.21s^{-1}
Dynamic Viscosity at 170.23s^{-1}
Dynamic Viscosity at 340.46s^{-1}
Dynamic Viscosity at 510.69s^{-1}
Dynamic Viscosity at 1021.38s^{-1}
μ [cP]
T [°F]
5,000 psi
10,000 psi
20,000 psi
30,000 psi
40,000 psi

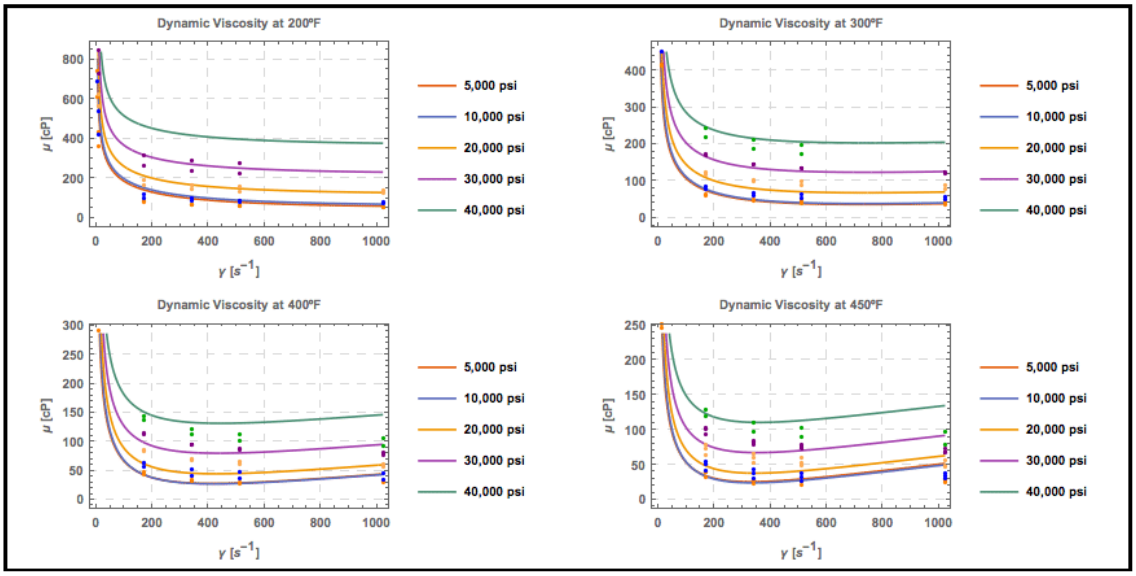
Dynamic Viscosity at 200°F
Dynamic Viscosity at 300°F
Dynamic Viscosity at 400°F
Dynamic Viscosity at 450°F
μ [cP]
γ [s^{-1}]
5,000 psi
10,000 psi
20,000 psi
30,000 psi
40,000 psi

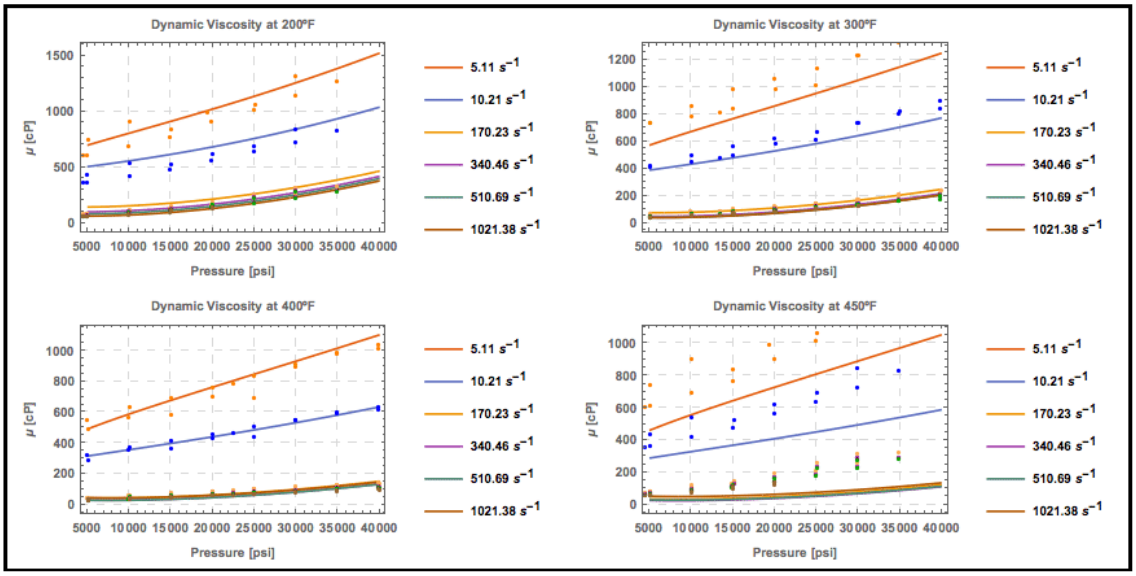
Dynamic Viscosity at 200°F
Dynamic Viscosity at 300°F
Dynamic Viscosity at 400°F
Dynamic Viscosity at 450°F
μ [cP]
Pressure [psi]
5.11 s−1
10.21 s−1
170.23 s−1
340.46 s−1
510.69 s−1
1021.38 s−1

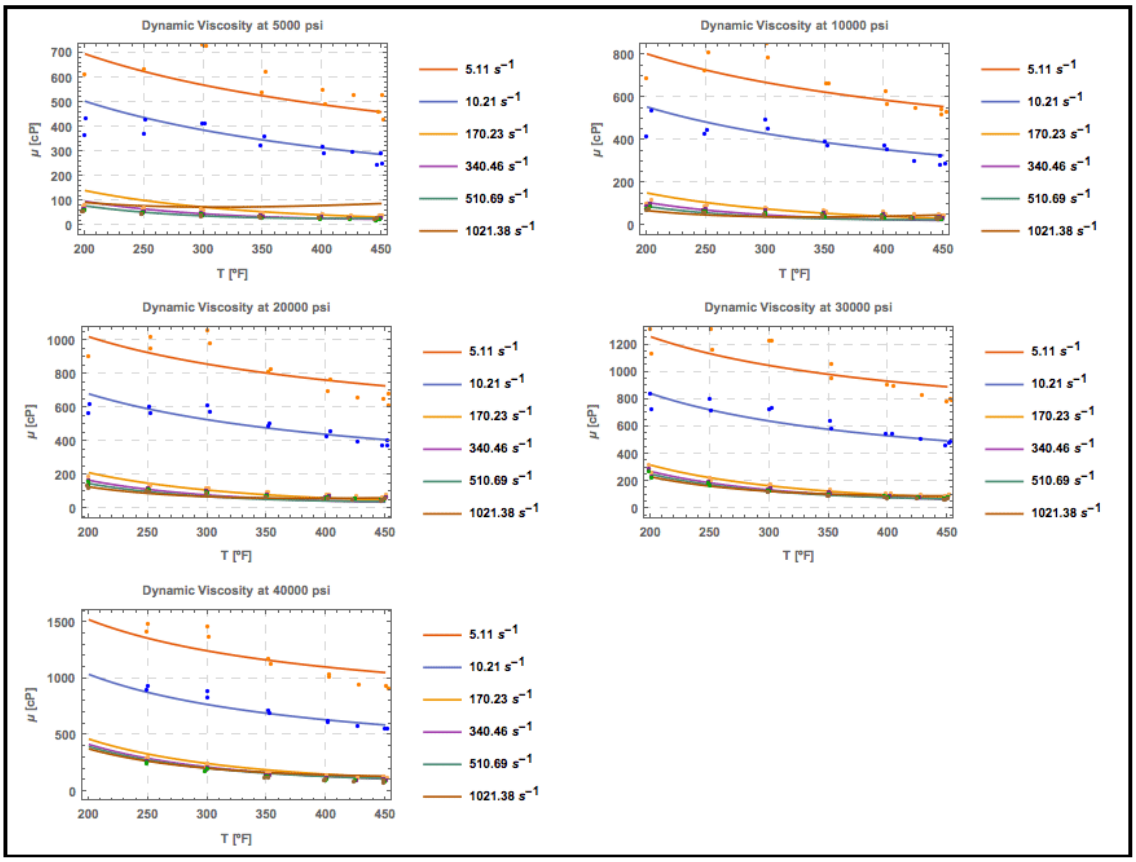
Dynamic Viscosity at 5000 psi
Dynamic Viscosity at 10000 psi
Dynamic Viscosity at 20000 psi
Dynamic Viscosity at 30000 psi
Dynamic Viscosity at 40000 psi
μ [cP]
T [°F]
5.11 s−1
10.21 s−1
170.23 s−1
340.46 s−1
510.69 s−1
1021.38 s−1

APPENDIX D

3D graphs for shear stress.

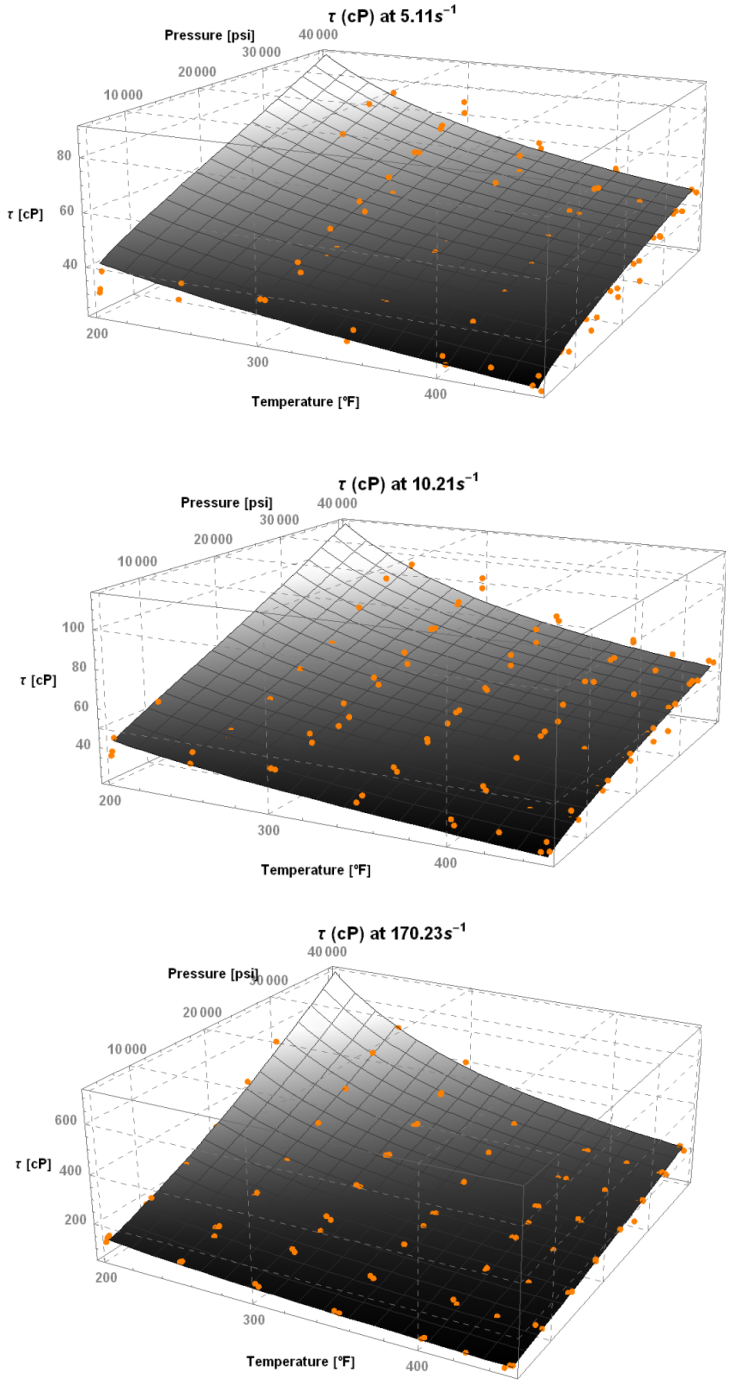

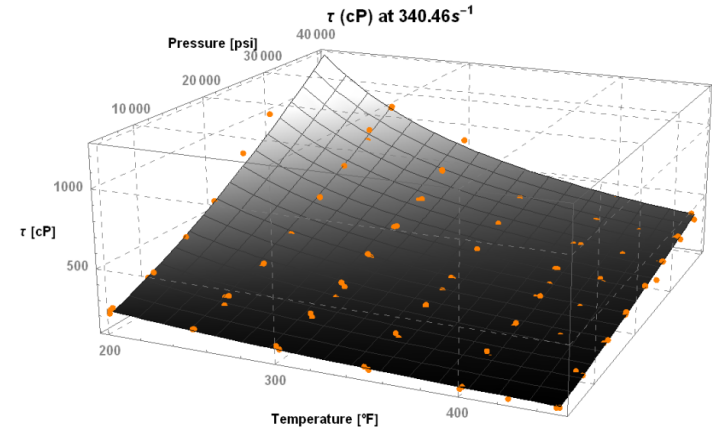
τ (cP) at 340.46s⁻¹
Pressure [psi]
40 000
30 000
20 000
10 000
1000
τ [cP]
500
200
300
400
Temperature [°F]

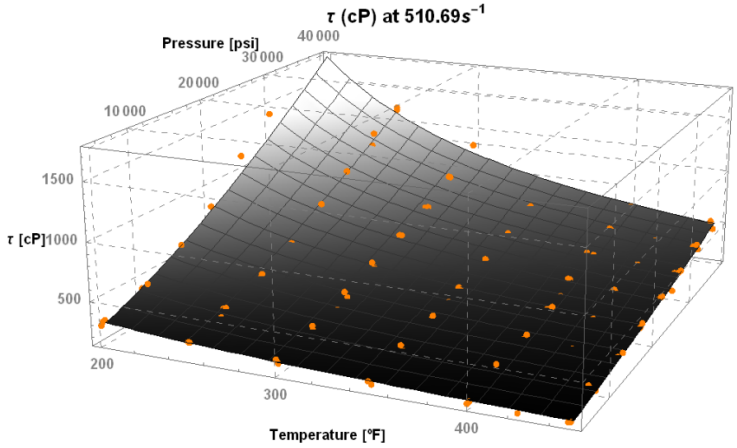
τ (cP) at 510.69s⁻¹
Pressure [psi]
40 000
30 000
20 000
10 000
1500
τ [cP]
1000
500
200
300
400
Temperature [°F]

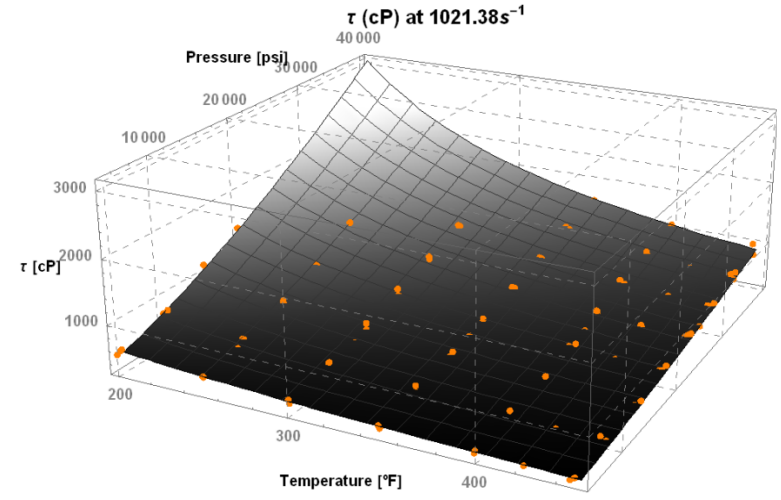
τ (cP) at 1021.38s⁻¹
Pressure [psi]
40 000
30 000
20 000
10 000
3000
τ [cP]
2000
1000
200
300
400
Temperature [°F]

APPENDIX E

Cross sections of 3D graphs for shear stress.

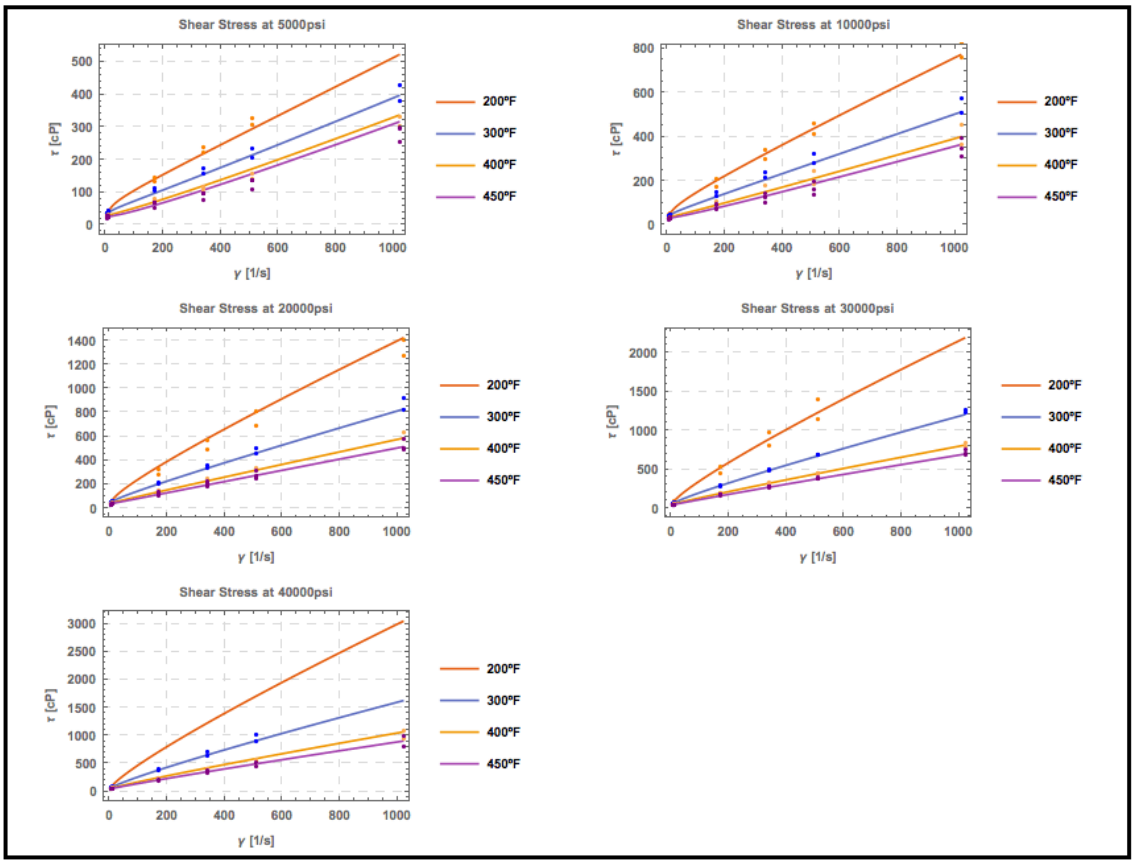

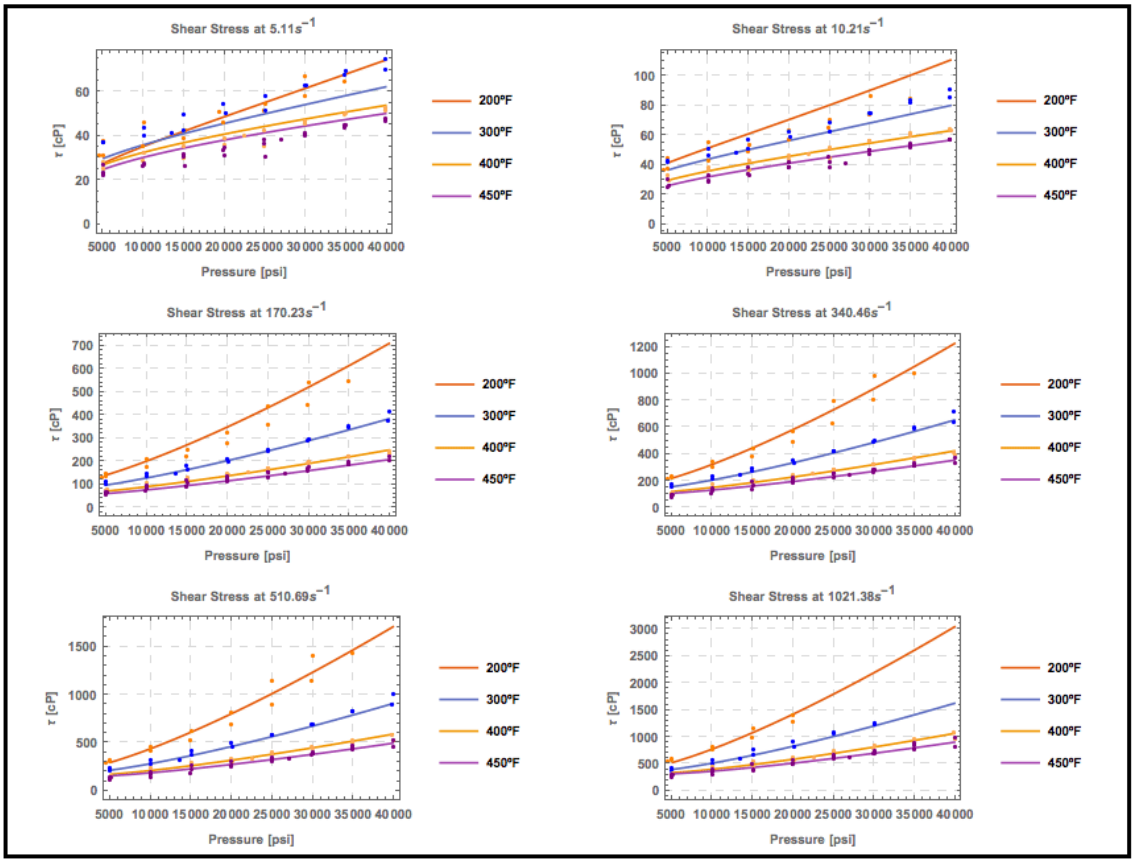
Shear Stress at 5.11s^-1
Shear Stress at 10.21s^-1
Shear Stress at 170.23s^-1
Shear Stress at 340.46s^-1
Shear Stress at 510.69s^-1
Shear Stress at 1021.38s^-1
τ [cP]
Pressure [psi]
200°F
300°F
400°F
450°F

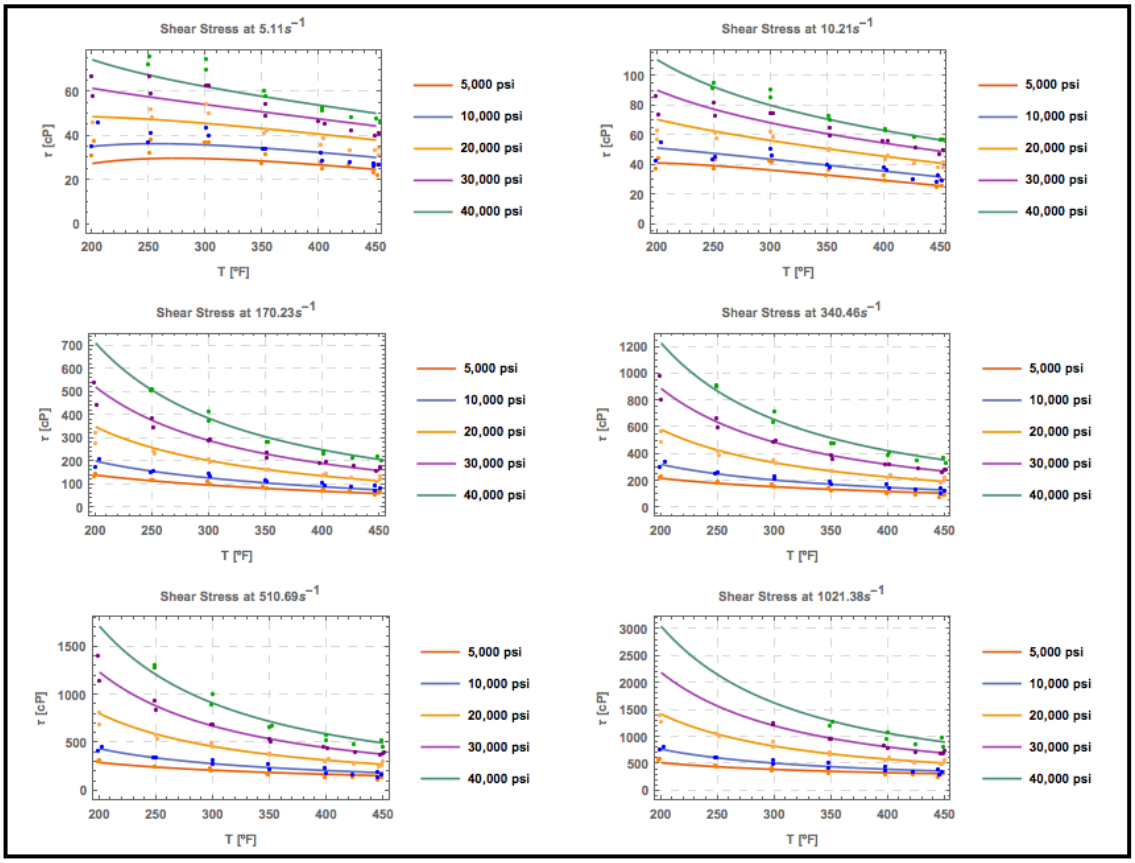
Shear Stress at 5.11s^-1
Shear Stress at 10.21s^-1
Shear Stress at 170.23s^-1
Shear Stress at 340.46s^-1
Shear Stress at 510.69s^-1
Shear Stress at 1021.38s^-1
τ [cP]
T [°F]
5,000 psi
10,000 psi
20,000 psi
30,000 psi
40,000 psi

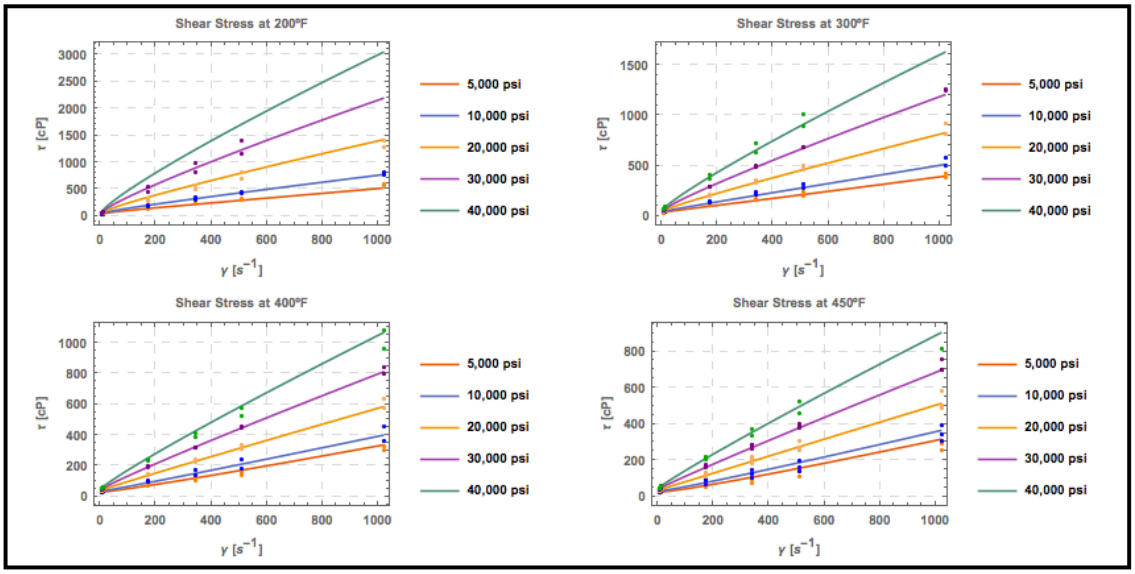
Shear Stress at 200°F
Shear Stress at 300°F
Shear Stress at 400°F
Shear Stress at 450°F
τ [cP]
γ [s^-1]
5,000 psi
10,000 psi
20,000 psi
30,000 psi
40,000 psi

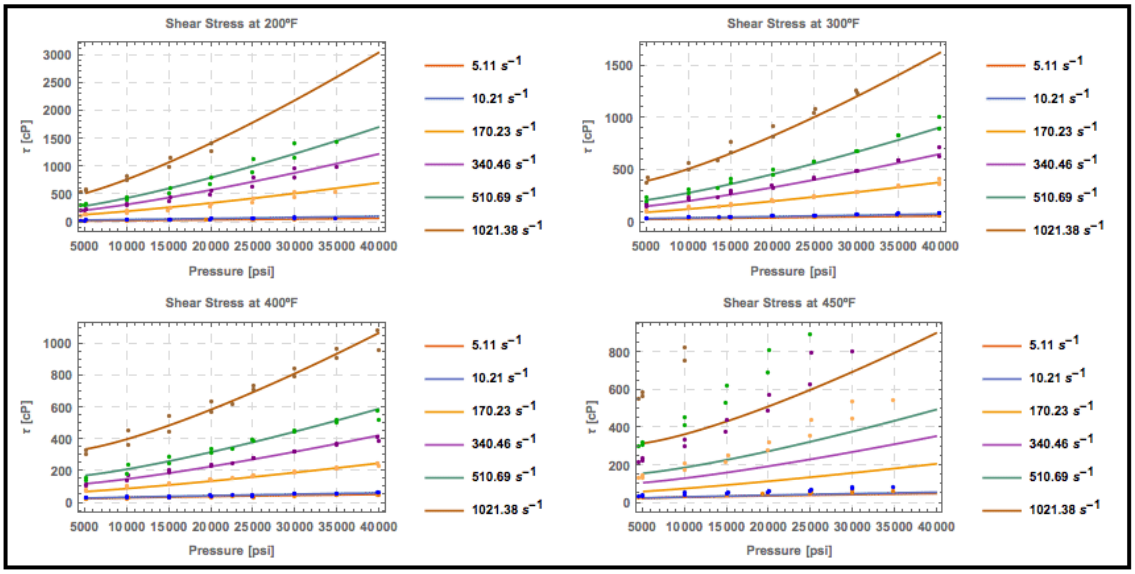
Shear Stress at 200°F
Shear Stress at 300°F
Shear Stress at 400°F
Shear Stress at 450°F
τ [cP]
Pressure [psi]
5.11 s−1
10.21 s−1
170.23 s−1
340.46 s−1
510.69 s−1
1021.38 s−1

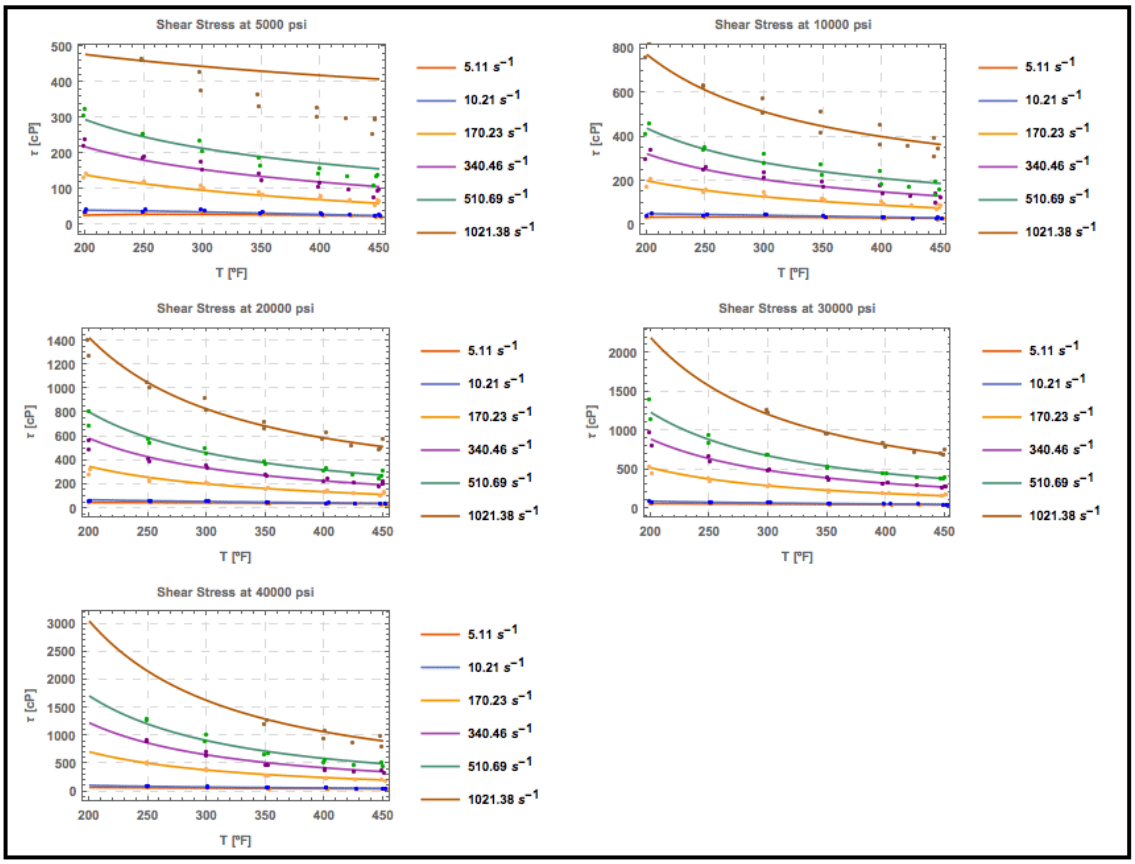
Shear Stress at 5000 psi
Shear Stress at 10000 psi
Shear Stress at 20000 psi
Shear Stress at 30000 psi
Shear Stress at 40000 psi
τ [cP]
T [°F]
5.11 s−1
10.21 s−1
170.23 s−1
340.46 s−1
510.69 s−1
1021.38 s−1